

Interphases, Interfaces, and Surfaces of Active Materials in Rechargeable Batteries and Perovskite Solar Cells

Chaofeng Liu, Jifeng Yuan, Robert Masse, Xiaoxiao Jia, Wenchao Bi, Zachary Neale, Ting Shen, Meng Xu, Meng Tian, Jiqi Zheng, Jianjun Tian,* and Guozhong Cao*

The ever-increasing demand for clean sustainable energy has driven tremendous worldwide investment in the design and exploration of new active materials for energy conversion and energy-storage devices. Tailoring the surfaces of and interfaces between different materials is one of the surest and best studied paths to enable high-energy-density batteries and high-efficiency solar cells. Metal-halide perovskite solar cells (PSCs) are one of the most promising photovoltaic materials due to their unprecedented development, with their record power conversion efficiency (PCE) rocketing beyond 25% in less than 10 years. Such progress is achieved largely through the control of crystallinity and surface/interface defects. Rechargeable batteries (RBs) reversibly convert electrical and chemical potential energy through redox reactions at the interfaces between the electrodes and electrolyte. The (electro)chemical and optoelectronic compatibility between active components are essential design considerations to optimize power conversion and energy storage performance. A focused discussion and critical analysis on the formation and functions of the interfaces and interphases of the active materials in these devices is provided, and prospective strategies used to overcome current challenges are described. These strategies revolve around manipulating the chemical compositions, defects, stability, and passivation of the various interfaces of RBs and PSCs.

consumption of fossil fuels and increasingly urgent environmental issues.^[1,2] Tremendous research effort has been invested developing various types of clean energy conversion and storage technologies; such intensive research activities have resulted in great recent progress in the development and commercialization of solar cells, wind turbines, rechargeable batteries (RBs), and supercapacitors.^[3–8] Rapid progress in metal halide perovskite solar cells (PSCs) represents an excellent example of the most recent and exciting developments in renewable energy conversion.^[9–15] Because of its tunable bandgap,^[16] high carrier mobility,^[17–19] large light absorption coefficient,^[20] and low formation energy,^[21] advances were able to rapidly boost the power conversion efficiency (PCE) from 3.8% in 2009 to 25.2% in 2019.^[9,22] Research contributions to each component have been indispensable to this progress—these advances include tuning the chemical composition and processing methods, control of the crystallinity and morphologies, and engineering surface/interface defects.^[23,24]

1. Introduction


Renewable energy generation and storage have both become important pieces of infrastructure required to enable a sustainably powered society, especially in light of the rapid

In spite of its widespread commercialization, progress in the advancement of RB technologies has been painstakingly slow but steady. Like PSCs, similar research efforts have been devoted to exploring new materials, controlling and tuning crystallinity and morphologies, and tailoring the surface and interface properties.^[25–28] Although battery materials and technologies have been studied for more than a century,^[3] many mysteries remain. Their complexity arises from the interactions of each component with another. Interfaces between structural materials (like current collectors and binders) and active materials must remain chemically and electrochemically stable, while interfaces at the electrodes and electrolyte must deliver good electrochemical properties.^[29,30] This involves both mass and charge transfers across the interfaces not only between electrolyte and electrodes but also between electroactive materials, carbon black, and possible coatings.^[31,32] Any irreversible reaction at the interfaces would lead to a change of surface chemistry and unavoidably affect the energy storage performance.^[33,34] In addition, the insertion and extraction of active ions during the charge–discharge process cause the expansion

Dr. C. Liu, R. Masse, X. Jia, W. Bi, Z. Neale, Dr. M. Xu, M. Tian, J. Zheng, Prof. G. Cao

Department of Materials Science and Engineering
University of Washington
Seattle, WA 98195, USA
E-mail: gzcao@u.washington.edu

J. Yuan, Dr. T. Shen, Prof. J. Tian
Institute for Advanced Materials and Technology
University of Science and Technology
Beijing 100083, China
E-mail: tianjianjun@mater.ustb.edu.cn

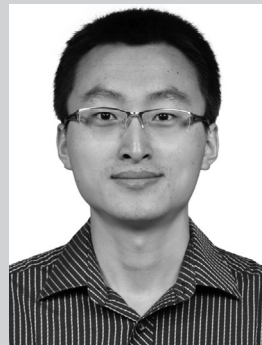
 The ORCID identification number(s) for the author(s) of this article can be found under <https://doi.org/10.1002/adma.201905245>.

DOI: 10.1002/adma.201905245

and contraction of the lattice of the active materials, which may result in microstructure degradation.^[35] Surface coatings and passivation are, thus, often introduced to the already complex electrodes, and further complicate the mass and charge transfer kinetics.^[36] It is no exaggeration that good fundamental understanding of strategies to control and tailor the interface properties is critical to the further advancement of both RBs and PSCs.

Metal halide perovskite materials have the general formula ABX_3 , where A is a monovalent cation (such as methylammonium (MA), formamidinium (FA), Cs or their mix), B = Pb, Sn, and X = Cl, Br, I. The state-of-the-art PSC configuration consists of multi-layers with a transparent oxide conduction layer, electron transport layer (ETL), active layer (halide perovskites), hole transport layer (HTL), and metal electrode. The perovskite layer generates excitons (hole–electron pairs) by absorbing photons, excitons separate into electrons and holes, which are transferred through ETL and HTL, respectively. The ETLs and HTLs are necessary to collect one charge carrier and block the other. To enhance the efficiency of PSCs, early studies focused on the selection and optimization of perovskite deposition technology to obtain perovskite films with good crystal quality and morphology.^[37–41] Interface modification and passivation of multi-layers in PSCs is one of the effective approaches to further increase the efficiency and stability of the solar cells.^[42,43] The charge carriers are unavoidably transported through several interfaces in the PSC. Besides the intrinsic nature of perovskite, the ETL and HTL interfaces also have a significant influence on the charge processes in devices. Interfacial defects and unmatched energy bands cause severe charge accumulation and recombination. Thus, interfaces with low trap states and closely matched energy bands are key to high-efficiency solar cells. The low formation energy of halide perovskites means that solution processing methods can be employed, leading to an inexpensive fabrication process with low-temperature annealing. Meanwhile, defects form at the grain boundaries and on the surface of the perovskite. First-principles calculations based on density functional theory (DFT) have shown that the majority of the defects have shallow energy levels,^[44,45] and are less effective in trapping carriers. However, some types of defects with deep energy at the interfaces of various layers act as Shockley–Read–Hall nonradiative recombination centers that shorten minority carrier lifetime and reduce the open current voltage (V_{OC}) of the solar cells.^[46] The stability of perovskite devices is also negatively affected by these ionic defects. A well-connected heterojunction with shallow trap states and minimal defects is an essential requirement to obtain high-performance PSCs.

Equally important as renewable energy generation is the efficient and economical storage of this energy.^[47–49] Based on the reaction mechanisms of the electrode material, energy storage systems can be divided into two groups: batteries and capacitors.^[30,50] RBs operate via reversible redox reactions at electrodes through ionic and electronic exchanges at their interfaces,^[51] while capacitors work via the adsorption of ions on the electrode interfaces.^[52] The rapid reaction kinetics in supercapacitors offers high power density while the high concentration of active sites in the crystal lattice of RBs endows them with high energy density. Taking advantage of both features, like in hybrid capacitors, is a compelling approach to achieve high power and energy density.^[53–56]



Chaofeng Liu earned his B.Sc. and M.Sc. degrees from Central South University and his doctoral degree from Beijing Institute of Nanoenergy and Nanosystems, Chinese Academy of Sciences. He is currently working as a postdoc at the University of Washington (Seattle). His research interests focus on

electrode materials for electrochemical energy storage, such as alkali-ion batteries and hybrid capacitors.



Jianjun Tian is a professor at the Institute for Advanced Materials and Technology, University of Science and Technology Beijing (USTB). He received his Ph.D. from USTB in 2007. During 2011–2012, he studied at the University of Washington. He built the Laboratory of Optoelectronic Materials and Devices in 2016 as leader (PI). He was nominated as director of Functional Materials Institute, USTB in 2015 and vice-dean of Institute for Multidisciplinary Innovation, USTB in 2019. His current research focuses on quantum dots and perovskites and their applications, including solar cells and light-emitting diodes.



Guozhong Cao is the Boeing–Steiner professor of Materials Science and Engineering, professor of Chemical Engineering and adjunct professor of Mechanical Engineering at the University of Washington, Seattle, WA. His current research focuses mainly on materials for energy conversion and storage.

The active components in a battery include the cathode and anode materials and the electrolyte, as schematically shown in **Figure 1a,b**. The cathode and anode materials accommodate working ions (e.g., Li^+ , Na^+ , or Mg^{2+}) and electrons to reversibly convert electrochemical energy into stored chemical energy.^[57–60] The electrolyte has the responsibility of transferring working ions between the cathode and the anode, while forcing electrons to pass through an external circuit to do work.^[61,62]

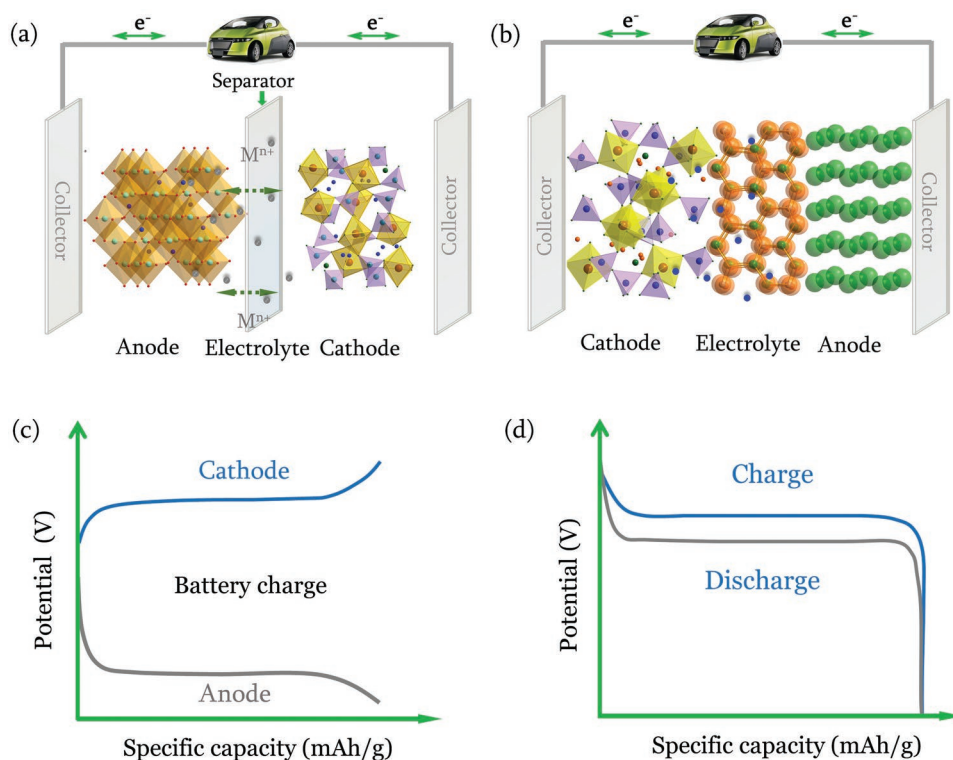


Figure 1. Configurations of a) liquid and b) solid-state batteries. Separator film and liquid electrolyte are replaced by an SSE in the latter case. However, the wettability of the active components in SSBs is a critical challenge. c) Energy density and d) energy efficiency of a battery. Energy density is determined by the specific capacity and working voltage of the battery. The chemical potentials of the cathode and the anode determine the battery voltage. Energy efficiency is defined by the ratio of discharging and charging energy densities, and reflects energy loss during battery operation.

A wide variety of strategies can be employed to increase battery efficiency and the amount of energy stored in the battery. To a first approximation, energy (in Wh) is equal to the voltage of the battery (in V) multiplied by its capacity (in Ah), as illustrated in Figure 1c. Therefore, a high redox potential from the cathode and the low chemical potential from the anode are prerequisites to achieving a high-voltage battery.^[63,64] Increasing the active sites and the number of reactive electrons increases the capacity of an active electrode material.^[65,66] Manipulating the crystal field or chemical bonds by defect engineering or controlling crystallinity can augment the redox potential of a given material.^[67,68] To improve the power capabilities of a material (a kinetic property), exposing active facets and reducing the particle size enhance the chemical activity for improving the ions storage capability.^[69–74] Designing electrolytes with higher oxidizing and lower reducing potential broadens the operating voltage window in nonaqueous high-voltage batteries.^[61,75–77] As for energy efficiency, the cell must approach 100% Coulombic efficiency to be a commercially viable technology. Given this assumption, energy efficiency will be defined by the ratio of energy output and input and is representative of the voltage gap between the charging and discharging processes (Figure 1d). This voltage gap is due to polarization caused by electrochemical kinetics and internal resistances.^[78] Minimizing these resistances and promoting the reaction kinetics of materials will help maximize the round-trip energy efficiency of the battery.^[79] To build a high-efficiency battery, whatever the materials or systems are chosen or designed,

the interactions between each component must be considered. Unfortunately, tradeoffs are often unavoidable.

For both PSCs and RBs, interfaces and surfaces play a significant role in determining redox reactions and mass and charge transfer, and thus determining the device performance. In this review, we take PSCs as a model system to discuss the impact of interfaces and surfaces on the charge transfer, PCE, and device stability. This review provides a detailed discussion of the achievements of interface modification, including bandgap regulation, promoting crystal growth of perovskite films, enhancement of charge mobility, defect passivation, and improvement of stability. For the RBs, we start with the discussion of the interphase formation between electrolytes and electrodes. The interphase in RBs plays a critical role, but is extremely complex owing to the wide variety of amorphous chemical species that are reduced or oxidized at the electrode surfaces. Because of the complexity associated with studying and characterizing these interphases, they receive far less attention than they deserve. We also discuss interface defects and surface energy, then artificial layer and space charge layer, prior to the discussion of PSC interfaces.

2. Interfaces and Interphases Formation in RBs

Typically, interphases are formed either in the first cycles or introduced by pretreatment on the surface of electrodes. The solid-electrolyte interphase (SEI) is designed to mitigate the side reactions between electrode materials and electrolyte,

especially in the case of Li-ion battery anode materials. Since graphite and other anode materials fall outside the stability window of today's state-of-the-art electrolytes, the SEI produced during formation cycling initially reduces the amount of active Li, but increases the energy and Coulombic efficiencies as well as the safety of batteries in the longer term.^[33,80–84] Beyond this, interfaces influence the wettability and compatibility of the battery components. Regulating the surface energy of the components can effectively modify their chemical activity or stability to broaden their electrochemical applications.^[85–87] In this review, we summarize the interfaces and interphases in liquid (aqueous and nonaqueous) and solid-state batteries by discussing the fundamentals of interphase formation and their function during battery operation. In addition, the current published models and compositions of interphases are also summarized. Several practical strategies on materials exploitation and system designs are proposed, for better battery operation and safety in the future.

The distinction between liquid (electrolyte) and solid-state batteries comes from the interfaces among their components. Solid–liquid interfaces determine the performance of batteries using liquid electrolytes. Wettability and chemical stability between the electrode and electrolyte becomes the important factors before batteries assembly (Figure 2a). In the solid-state batteries, solid–solid interfaces determine ion exchange

during battery operation. Lattice mismatch and chemical compatibility impact the power performance and lifespan of the battery (Figure 2b). Interfaces and interphases are essential in battery design and fabrication, while battery safety depends on the electrochemical compatibility between the electrolyte–cathode and the electrolyte–anode interfaces and thermal stability of individual components. Therefore, in the liquid batteries, the chemical potential of the cathode should sit higher than the highest occupied molecular orbitals (HOMO) of the liquid electrolyte (Figure 2c), otherwise an SEI, which in this case is also known as the cathode electrolyte interphase (CEI), will be formed on the cathode surface by the oxidized electrolyte. When the chemical potential of the cathode is lower than the HOMO, electrons from the electrolyte are injected into the 3d orbitals of redox-active cations in the cathode, typically a transition metal oxide.^[30,88–90] On the anode side, its chemical potential should be lower than the lowest unoccupied molecular orbitals (LUMO) of the liquid electrolyte (Figure 2c). This prevents the anode from reducing the electrolyte.^[30,57] However, the chemical potentials of lithium metal and graphite are higher than the LUMO of the carbonate-based electrolytes and result in the reduction of solvents and decomposition of lithium salt in nonaqueous Li-ion batteries.^[49,84,91] The SEI film formed on the surface of the anode is also called the anode electrolyte interphases (AEI) to distinguish it from the CEI.^[92]

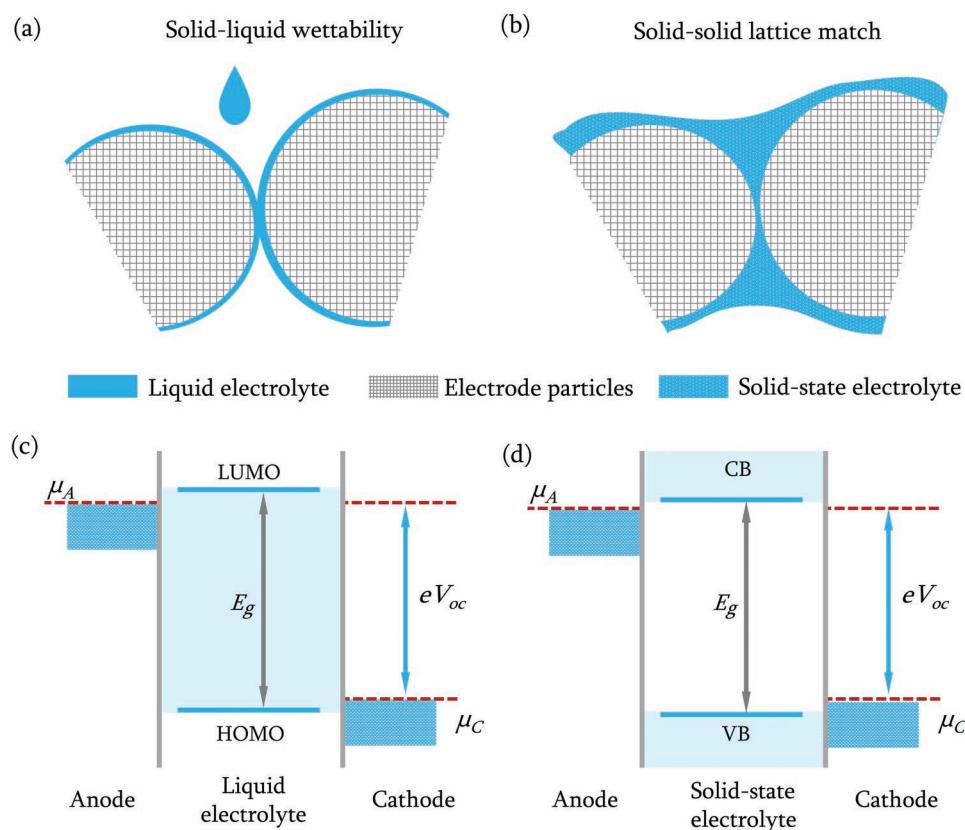


Figure 2. Interfaces in a) liquid and b) solid-state batteries. Solid–liquid interfaces determine ion migration and electron transfer in a liquid-electrolyte battery. Solid–solid interfaces in SSBs determine the battery operation. The chemical compatibility between the SSE and electrode materials is more difficult to manipulate. Schematics of the relationship between chemical potentials among active components in c) liquid and d) solid-state batteries. In principle, the chemical potentials of the cathode and the anode should be positioned within the gap between the HOMO and LUMO of the liquid electrolyte or the gap of VB and CB in an SSE, which ensures no side reactions occur between the electrolyte and the electrode materials.

In a solid-state battery (SSB), the relationship between the chemical potentials of the solid-state electrolyte (SSE) and the cathode and the anode should also obey these guidelines. Unlike the liquid electrolyte, the working voltage window of the SSE is defined by the gap between the valence band (VB) and the conduction band (CB; Figure 2d).^[30] From the viewpoint of solid-state physics, the overlap of molecule orbitals forms the VB and CB when the molecules stack periodically to construct a solid material.^[93] The same chemical principles apply otherwise. As shown in Figure 2d, the chemical potential of the anode should be lower than the CB of the SSE, otherwise the electrons will be injected into the CB and reduce the SSE. At the cathode, its chemical potential must be higher than the position of VB, otherwise the SSE will lose electrons and trigger side reactions with the cathode.^[30] The side reactions between the SSE and the cathode or the anode may produce some interphases (impurities) or ions exchange at the interfaces, which causes mismatch between the crystal lattices,^[94–96] and even form cracks in the battery.^[97–100]

Typically, the interphases formed in either liquid or solid-state battery, are ionic conductors but electrical insulators.^[33,83] In liquid-electrolyte batteries, an SEI will inhibit direct contact between the liquid electrolyte and electrode materials, and prevent further side reactions.^[61,84] Because the amount of liquid electrolyte is rigorously controlled, the consumption of electrolyte by the formation of SEI will decrease the practical capacity and energy density. A thinner and denser SEI is preferred when it is unavoidable. The solvents and salts in the liquid electrolyte also affect the compositions of the SEI and by extension, the battery performance.^[33,101] The situation in SSB is possibly more complex because the interphases could be ionic and electrical insulators, which result in higher resistances or even crystal lattice distortion between the difference phases, and causes the battery to breakdown.^[99,102,103] In literature, CEI and AEI, as mentioned above, are sometimes used to describe the SEI on the cathode and the anode, respectively, but we adopt the term “SEI” in this review to avoid confusion.

3. Models and Compositions of Interphases in RBs

Interphases form when side reactions are triggered by the mismatch of chemical potentials between the electrolyte and the electrode materials. For liquid-electrolyte batteries, the SEI consists of two groups of components, one is organic and the other is inorganic. The organics originate from the decomposition of solvents from the electrolyte, such as esters and ethers.^[104,105] The inorganics are derived from salt decomposition, usually containing fluorides, oxides, and carbonates.^[106] Elemental analysis easily identifies the functional groups in the SEI film, but it is difficult to verify the exact phases. The SEI film is a composite, with complex composition distribution and structure, and could be significantly affected by the solvents and additives. To elucidate ion migration and other beneficial effects of the SEI, several assumptions and models have been proposed to describe the possible configurations and compositions. The models at solid–liquid and solid–solid interfaces will be summarized separately in this section.

The difference in chemical activity of the electrode materials and the electrolyte causes the formation of SEI in liquid-electrolyte batteries. For example, at the anode side, the highly active lithium metal attacks the solvents in electrolyte,^[107] and the chemical potential of graphite sits above the LUMO of the electrolyte to donor electrons and reduces the electrolyte.^[30] Graphite has been a successful anode material for commercial Li-ion batteries because its layered structure provides active sites to host Li ions and it has a low potential for reversible lithium intercalation and extraction.^[108,109] Based on the distribution of the compositions, initial formation of the SEI is believed to be composed of two layers^[106,110] as shown in Figure 3a. The compact inorganic layer (≈ 2 nm thick) is adjoined to the surface of the electrode materials, and the porous organic layer (≈ 100 nm thick) contacts bulk electrolyte.^[83,111,112] Further studies established a widely accepted model of the SEI, the Mosaic structure (Figure 3b).^[113] In this model, the electrode surface is first covered by a thin and compact inorganic layer, followed by a mixture zone consisting of inorganic and organic species. Thermodynamically stable inorganic species such as LiF, Li₂CO₃, and Li₂O are formed preferentially since they are compatible with the lithium metal or graphite anodes in Li-ion batteries.^[114] The chemical compatibility between organic species and bulk electrolyte improves the wettability, and in turn the composition of the SEI will influence the electron transfer and ion transfer resistances in the battery. Generally, the anions

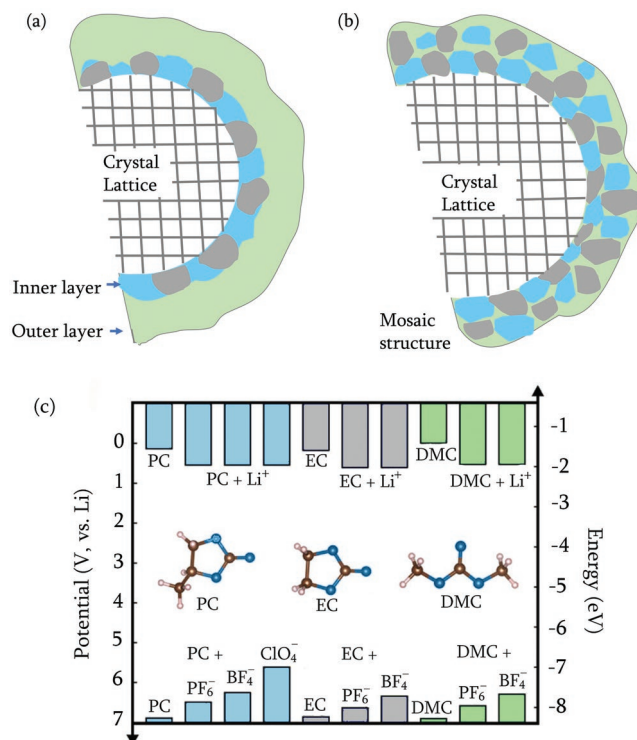


Figure 3. Models of the SEI in liquid batteries. a) Two-layer model: the inner layer is inorganic component and the outer one is the polymer-like gel and b) mosaic model: the SEI contains multiple inorganic and organic layers, though the thin inorganic layer covers the electrode first as assumed in the two layers model. c) Reducing and oxidizing potential of solvents and salts in Li-ion batteries calculated by DFT. Adapted with permission.^[131] Copyright 2015, American Chemical Society.

from the salts and the solvent molecules in the electrolyte determine the compositions of the inorganic and organic species, respectively.^[34] The anions in lithium salts have a strong impact on the impedance of the SEI. For example, LiF is highly resistive, and increasingly resistive LiF films will form according to this order of electrolyte salts: $\text{PF}_6^- > \text{SO}_3\text{CF}_3^- \sim \text{BF}_4^- > \text{AsF}_6^- > \text{ClO}_4^-$.^[115,116] In ether solvents, the organic species in the SEI are mainly alkoxides and carboxylates,^[117,118] while semicarboxylates and dicarbonates dominate the SEI composition in ester solvents.^[119–121] Although organic species are not considered to have a significant effect on SEI impedance, their reversibility affects the specific capacities of conversion-type anodes.^[122–124] Recently, the decarbonate species that were believed to play an important role in the SEI have been verified as monocarbonate species. Monocarbonates have an ionic conductivity of $\approx 10^{-6} \text{ S cm}^{-1}$, while dicarbonates are almost ionic insulators.^[125] This discovery suggests a full understanding of the SEI remains uncertain, and new methods and techniques are required for further discoveries. Apart from the solutes and solvents, the nature of the electrode materials also has an impact on the distribution and composition of the SEI. Highly oriented pyrolytic graphite possesses distinct basal and edge planes and is beneficial for studies on the thickness and compositions of the SEI. Solvated salts are suggested to intercalate and decompose at the edges, which are the inlet and outlet for ion exchange between the electrode and the electrolyte.^[126,127] Faster electron transfer at the edge is believed to accelerate electrolyte decomposition at the initial operation of batteries.^[128,129] The thickness of the SEI on basal planes continuously increases, but at edge plane does not change after the first cycle,^[112,130] verifying the edge planes helps with the formation of complete SEI and preventing side reactions in the subsequent cycling. At the cathode side, when the HOMO of the electrolyte is lower than that of most cathodes, there is inadequate thermodynamic driving force to trigger the decomposition of the electrolyte.^[131] The SEI film has the similar components as the SEI when formed in the electrolyte containing the same salts and solvents. Generally, the oxidizing potentials of the solvents and salts are higher than the upper cut-off voltages of the common cathodes (Figure 3c),^[131] therefore, the electrolyte is comparatively harder to oxidize at the cathode during the charging process. However, the surface chemistry of the cathode materials can drive nucleophilic attack to decompose the electrolyte. For example, in Li-rich layered cathodes, upon charging, the lattice oxygen can donate electrons to produce superoxide, which can attack carbonate molecules to form lithium carbonate (Li_2CO_3) in the SEI.^[132] The detected semicarboxylates on the surface of LiMn_2O_4 also suggest the decomposition of the carbonate solvents.^[133] Additives such as vinylene carbonate and fluoroethylene carbonate are used to counteract these side reactions and they form a thin and stable SEI to enhance batteries' efficiency and safety.^[76,134,135] Additionally, an additional artificial layer or coating can form a protective SEI that suppresses surface phase transitions and dissolution of the cations.^[136]

The main benefit of SSBs is that they overcome the safety issues in nonaqueous batteries—namely, the fire hazard they pose because of their flammable organic electrolytes.^[107,137,138] Further, this would (in principle) enable the use of Li-metal anodes, which have long been proposed as an alternative to

graphite and lead to even higher energy density batteries. Unlike liquid batteries, SSBs depend on solid–solid interfaces where the “wettability” depends on coherent lattice matching between the electrode and electrolyte. Critical goals to enable practical SSBs include 1) lowering the resistance and 2) increasing the stability of the interfaces, and 3) mitigating dendrite penetration along grain boundaries of the SSE.^[139–143] Figure 4a illustrates the possible contacts at the solid–solid interface in SSBs. Under ideal conditions, the interface contact between electrode and SSE should be coherent. However, it is difficult to find electrode materials and SSEs with the same lattice parameters. Further, the strain and stress from lattice expansion or shrinkage, caused by lithiation and delithiation, respectively, could induce cracks in the electrode, or even peel the electrode off.^[97,144] Lattice mismatch appears in most of solid-state systems, such as oxygen-ion conductors. However, in that case the dislocation defects caused by lattice mismatch are beneficial for the ion migration.^[145,146] Furthermore, in a Li-ion SSB, a slight lattice mismatch and distortion could also reduce the activation energy for ion migration and enhance ionic conductivity in epitaxial Garnet ($\text{Li}_7\text{La}_3\text{Zr}_2\text{O}_{12}$, LLZO) thin-film electrolyte.^[147] The disordered zone formed at the interface derives from the chemical instability of the electrode material and the SSE. For example, at the $\text{LiCoO}_2/\text{LiPON}$ interface, the surface disorder of LiCoO_2 increases the interfacial impedance. Upon cycling, the accumulation of lithium byproducts (such as Li_2O_2 and Li_2O) and the formation of CoO increase the thickness of the interfacial layer and decrease the battery's lifespan.^[148] It seems contradictory that the effects of interface mismatch in the examples of LiPON and LLZO mentioned above benefit one and hurt the other. An in-depth understanding on interface distortion and identifying if there is a critical threshold for beneficial performance should be studied to better understand the balance between electron scattering and ion migration at the disordered zone. To overcome the chemical instability between the SSE and the electrode materials, an artificial interlayer can be introduced to decrease the interfacial impedance. One good example is NbO_2 buffering layer on LiCoO_2 , which improves the chemical stability of SSBs by buffering the change of Co–O bond length and lowering strain/stress at the interface during battery cycling.^[149] The artificial interphase also improves the wettability of the SSE with the Li metal anode. By comparison, garnet electrolytes have superior ionic conductivity ($\approx 10^{-3} \text{ S cm}^{-1}$) and good chemical stability against the Li metal anode, but its poor wettability significantly limits its applications.^[150] Another study demonstrated that deposition of a thin Al interlayer on the surface of the garnet electrolyte could change Li wettability by forming a Li–Al alloy (Figure 4b,c), leading to a nearly 13-fold decrease in the interfacial impedance, from $950 \text{ } \Omega \text{ cm}^2$ at the pristine sample to $75 \text{ } \Omega \text{ cm}^2$ in the modified electrolyte.^[151] Meanwhile the wettability between garnet-type electrolytes and the cathode can be solved with an asymmetric solid electrolyte—i.e., by including an additional polymer electrolyte layer between the cathode and garnet electrolyte (Janus configuration) as shown in Figure 4d. The polymer electrolyte easily wets the cathode materials and has intimate contact with the garnet electrolyte and the gentle tension at the Li/polymer interface prevents nucleating of dendrites.^[152] These results indicate that surface modifications and the Janus configuration enhance

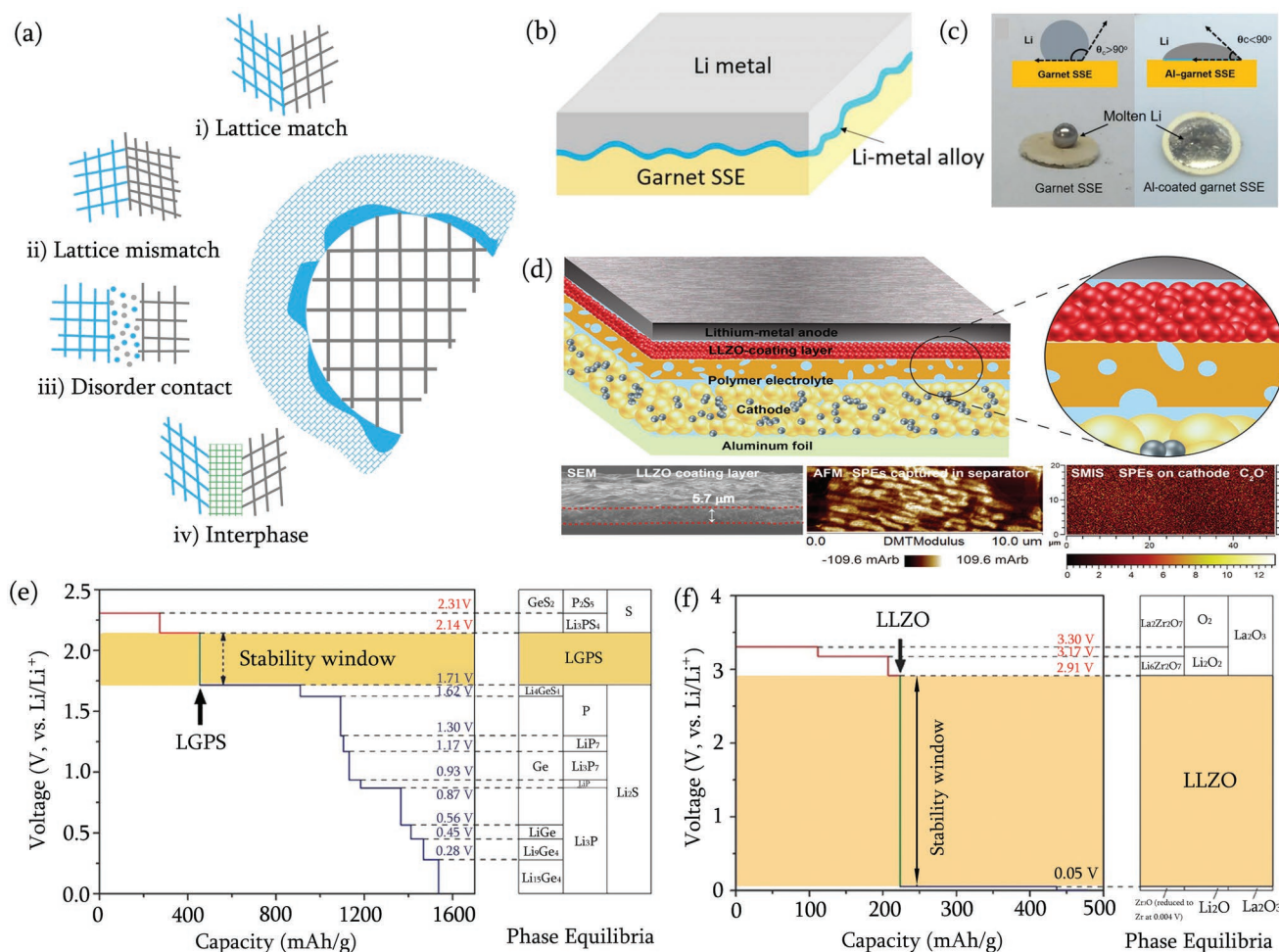


Figure 4. a) Models of the interphases in solid-state batteries. Four possible contact models between SSE and electrode materials. i) Lattice match: an ideal situation where both materials have the same lattice parameters. ii) Lattice mismatch: the differences between lattice parameters induce dislocations at the interface between the SSE and the electrode materials. iii) Disordered contact: a disordered zone contains atoms penetrating from each side. iv) Interphases: a new phase forms at the interface. The new phase may be conductive or insulating to both ionic or electronic transport. b) Schematic of the artificial layer between a garnet electrolyte and Li metal anode. Reproduced with permission.^[151] Copyright 2017, AAAS. c) Comparison of Li wettability on a garnet electrolyte without and with a thin (20 nm) Al layer. Reproduced with permission.^[151] Copyright 2017, AAAS. Alloying between Li and Al improves the Li wettability on the garnet electrolyte and makes intimate interfacial contact in SSBs. d) Janus SSE comprised of organic and inorganic layers. Reproduced with permission.^[152] Copyright 2018, American Chemical Society. One prevents dendrites from the metallic anode and the other ensures the wettability with the cathode particles. Voltage profile and phase equilibria of e) LGPS and f) LLZO solid electrolyte upon lithiation and delithiation calculated from first principles. Adapted with permission.^[155] Copyright 2016, Wiley-VCH. These diagrams provide routes for their surface modifications. The theoretical voltage windows are narrower than the experimental results because the weak current from electrolyte decomposition is drawn out by the strong current signal forms Li plating and stripping. Adapted with permission.^[155] Copyright 2016, Wiley-VCH.

the chemical stability and compatibility of SSE with adjacent components. Being classified as a new interphase, the ionic resistive disorder zone is very challenging, although sometime the formation and decomposition process is reversible.^[153] Controlling the compositions and taking advantages of the reversibility of the interphases maybe explore a novel strategy to improve SSB performance.

Phase equilibria diagrams of the SSE under the lithiation and delithiation provide guidance for practical applications of the SSE and for modifying it. Figure 4d,f illustrates the voltage profiles and phase diagrams of $\text{Li}_{10}\text{GeP}_2\text{S}_{12}$ (LGPS) and LLZO, respectively. These results have shown that during the lithiation process, LGPS is decomposed into Li-Ge alloys, Li-P compounds, and Li_2S ,^[154] and LLZO transforms into $\text{La}_2\text{Zr}_2\text{O}_7$,

$\text{Li}_6\text{Zr}_2\text{O}_7$, and Li- and La-oxides when the voltage exceeds 2.91 V.^[155] This suggests that LGPS and LLZO have narrower operating voltage windows than the reported 0.0–5.0 V.^[156,157] The differences between computation and experiments are attributed to the small current derived from the electrolyte decomposition, while the signal from Li plating and stripping is significant.^[155] In addition, crystalline LLZO poses a potential safety risk because Li dendrites can grow along the grain boundaries when the current distribution is uneven during battery operation.^[140,158] Goodenough and co-workers suggest that amorphization of the SSE could effectively eliminate the grain boundaries and suppress dendrite penetration.^[159–161]

Changing the lattice orientation exposes different ion diffusion channels of the electrode materials, which impacts redox

reactions in SSBs. LiCoO₂ with exposed (110) planes was deposited on a Li₂O-coated Al current collector to suppress the formation of the Li-deficient phase Co₃O₄, resulting in an enhanced ion diffusivity and rate capability in an all-solid-state thin-film battery.^[162] Controlling the interfaces to avoid the formation of ionic resistive interphases, or introducing buffering layers to improve the interfacial contact and chemical compatibility among battery components is an effective strategy to deal with the critical challenges hindering the commercialization of SSBs. Creeping of metallic Li also dominates Li transportation at the interface of SSB under a critical stripping current density^[163] and a considerable pressure applied on SSB may have achieved a modest power density in practice as well.

4. Concerns and Strategies in RBs

Advanced understanding and control of the interfaces of battery materials help generate hypotheses for improving their electrochemical performance. These interfaces will be influenced by surface defects, and surface energy for ion intercalation, and electrolyte wettability, which in turn impact surface phase transitions (such as in ternary cathodes) or side reactions (like those that form the SEI layer on Li-metal anodes). In this section, we focus on the interfacial engineering for enhancing electrochemical activity and chemical stability.

4.1. Interface Defects and Surface Energy

When the battery is assembled, the solid–gas interface at the electrodes is replaced with solid–liquid or solid–solid interfaces. Nanotechnology opens a door to reduce the particle size and expose specific facets and break the anisotropy of electrode materials that promote electrochemical activity. These advantages at the nanoscale enable some electrochemically inactive micro-sized materials to become capable of hosting ions and storing energy.^[164–166] Surface engineering techniques such as doping^[167–169] and atmospheric treatment^[170,171] modify the surface energy and wettability by regulating the surface composition and character of chemical bonds. Typically, chemical doping introduces defects in both the bulk and surface.^[168] However, in the following section, we focus only on surface defect introduction through atmospheric treatment and its impacts on surface materials chemistry. Surface passivation or gradient compositions have similar effects as doping, which will be discussed in the following section “Artificial layer and space charge layer.”

Surface hydrogenation introduces oxygen vacancies that enhance the electrical conductivity and surface energy. This leads to accelerated redox reactions, as verified in Ti-oxide anodes^[171–176] and V-oxide cathodes.^[85,170] Anatase TiO₂ has been proposed as a promising anode material for Li-ion batteries due to high theoretical specific capacity of 335 mAh g⁻¹ and flat voltage profile.^[171] However, the compact atom stacking and the poor intrinsic electrical conductivity limit its reaction kinetics during Li-ion intercalation. Hydrogenation produces a disordered layer on the particle surface, which alleviates structural distortion during the lithiation and delithiation process. Meanwhile the overlapping of atomic

orbitals in the disordered layer becomes weaker and causes a weaker interaction between the transferred electrons and host lattice, resulting in enhanced electron transport in the electrode material.^[171] The high mobility of hydrogen is responsible for the improved lithium storage capability. NMR spectra shown in **Figure 5a** detect two additional peaks around a chemical shift of 0 ppm, indicating dynamic exchange of ¹H. The easy replacement of H by Li results in the enhanced Li-ion storage.^[171] Low temperature electron paramagnetic resonance (EPR) spectra (**Figure 5b**) shows stronger signals with decreasing particle size. The stronger signal from unpaired electrons suggests that a higher concentration of oxygen vacancies is present at smaller particle sizes. More oxygen vacancies in turn suggest greater reduction of Ti⁴⁺ in the hydrogenation process.^[172] Calculations on the defect concentration in hydrogenated TiO₂ reflect the electrical and ionic conductivities as a function of hydrogenation time (**Figure 5c**). Surface hydrogenation affects the concentration of Li-ion carriers in the Li_xTiO_{2-δ} model. The interstitial Li ions are likely associated with excess electrons in the lattice to form the neutral species, which effectively decreases the concentration of free Li-ions. As hydrogenation proceeds, the greater degree of reduction, more neutral species form, and less free Li ions remain in the lattice.^[173] This is why the hydrogenation causes an increased electrical conductivity but a decreased ionic conductivity. Another thing to be noticed is that Li-ion conductivity is not the same as the Li-ion diffusion coefficient. The ionic diffusion coefficient increases with the time of hydrogenation but then decreases after 5 h^[173] because overall ion diffusion relies on the concentrations of both ionic and electronic carriers. Ti³⁺ is also detected in hydrogenated Li₄Ti₅O₁₂^[176] or CO-treated TiO₂,^[177] which provides a junction for fast electron transfer and improved rate capability. However, hydrogenated TiOF₂ exhibits different physical properties, even though oxygen vacancies are introduced in the host lattice. *I*–*V* curve measurements show that hydrogenated TiOF₂ has a higher resistance ($2.74 \times 10^{12} \Omega \text{ m}^{-1}$), than the untreated sample ($1.91 \times 10^{12} \Omega \text{ m}^{-1}$). The carrier density in hydrogenated TiOF₂ is also lower than the pristine sample, as seen by comparing the slopes of Mott–Schottky plots. The improved electrochemical performance of hydrogenated TiOF₂ is attributed to the existence of the fluorine rather than oxygen vacancies, which causes the disassociation of pristine TiOF₂ along the (001) direction to obtain a larger redox-active surface area.^[175]

Analogous to hydrogenation, surface sulfurization leads to partial delocalization of S 3p states in TiO₂. By broadening the VB and decreasing the band gap from 3.0 to 2.6 eV, reaction kinetics for sodiation were improved.^[178] In another sodium-based system, Fe₂O₃ was treated with a surface sulfurization technique. The authors measured a built-in electric field (BEF) using Kelvin probe force microscopy and believe that the BEF provides an additional driving force for sodiation and desodiation. During discharge (sodiation), the BEF Na-ion forms Fe₂O₃ (n-type) to FeS₂ (p-type) in the sodiation process, while upon charging the BEF is reversed and facilitates desodiation.^[179] It is controversial that Na-ion should cross the FeS₂ layer to reach the internal Fe₂O₃ core during sodiation, and it is not clear that the designed heterojunction fully explains the enhanced performance, but the sulfurized surface nevertheless displayed lower charge transfer resistance and improved electrochemical performance.

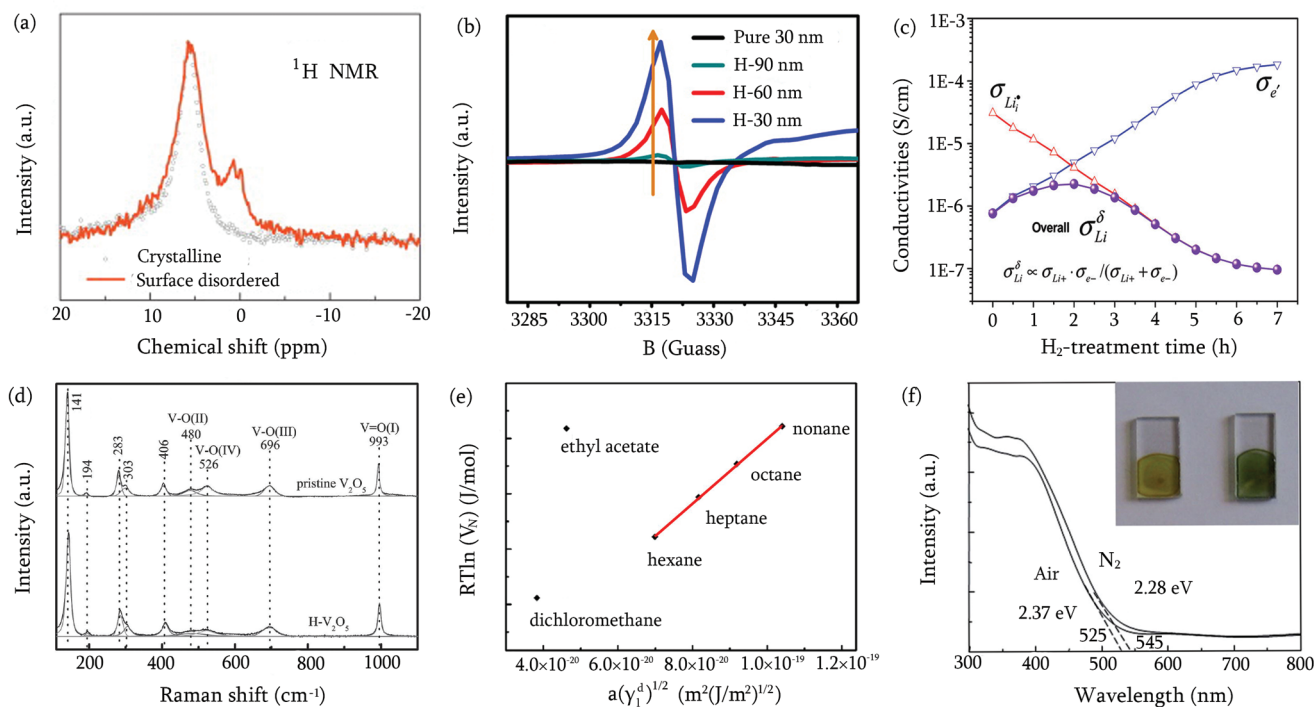


Figure 5. a) NMR spectra of crystalline and surface-disordered TiO_2 . Hydrogenation causes the surface defects and the additional peaks indicate the dynamic exchange of ^1H . Reproduced with permission.^[171] Copyright 2013, Elsevier. b) Low-temperature EPR spectra of pure TiO_2 with a size of 30 nm and hydrogenated TiO_2 with three different particle sizes. The strong signal indicates unpaired electrons arising from the appearance of oxygen vacancies. Adapted with permission.^[172] Copyright 2016, American Chemical Society. c) Calculated electrical (blue) and ionic (red) conductivities and overall ambipolar conductivity of Li ion (purple) from the defect model of $\text{Li}_x\text{TiO}_{2-\delta}$. Adapted with permission.^[173] Copyright 2012, American Chemical Society. Surface hydrogenation creates interstitial Li ions that are associated with excess electrons, leading to concentration fluctuations of ions and electrons. d) Raman spectra of pristine and hydrogenated V_2O_5 . Adapted with permission.^[170] Copyright 2016, Wiley-VCH. The intensity of the peak at 480 cm^{-1} decreased by 35%, suggesting that the oxygen vacancies formed on this bridge O site. e) Plots of $RT \ln(VN)$ versus $a(\gamma_d)^{1/2}$ of hydrogenated V_2O_5 . Adapted with permission.^[85] Copyright 2016, American Chemical Society. The slope of the fitted line is used to calculate the dispersive component of the overall surface energy. f) Absorption spectra of V_2O_5 films treated in air and nitrogen. The inset shows the films after annealing in air (left) and nitrogen (right). Adapted with permission.^[185] Copyright 2009, RSC. The reduced band gap implies the reduction of V^{5+} when the V_2O_5 film is annealed in nitrogen.

In V_2O_5 , defects such as oxygen vacancies have also been introduced through hydrogenation, but the exact position of the lost oxygen in the host lattice remains unclear. Raman spectra measure the vibration of chemical bonds and can be used to help clarify the lattice position of defects. In Figure 5d, hydrogenated V_2O_5 showed a similar Raman signal compared to the untreated sample. However, the intensity of the peak at 480 cm^{-1} decreased by 35%, suggesting the partially bridging oxygen bond that connects adjacent $[\text{VO}_5]$ pyramids is greatly weakened. In the hydrogen atmosphere, hydrogen is preferentially adsorbed at the oxygen sites to form OH groups. OH groups formed by the bridge oxygen and hydrogen are easier to remove compared to other lattice OH groups.^[170] In other words, the bond length of bridge O–V (2.02 \AA) is the longest in the $[\text{VO}_5]$ pyramid,^[180] which means there is less overlap between atomic orbitals and weaker bond strength. The formation of oxygen vacancies on the particle surface inevitably changes the surface chemical state of V_2O_5 , as shown from surface energy analysis using inverse gas chromatography (Figure 5e).^[85–87] The slope of the fitted line corresponds to the dispersive surface energy.^[181–183] Hydrogenated V_2O_5 has a higher total surface energy (63 mJ m^{-2}) than the pristine sample (40 mJ m^{-2}).^[85] This result makes sense since more

oxygen vacancies at the interfaces mean more dangling bonds and higher surface energy.

Electrical conductivity can be changed by modulating the band gap of a given material. In another surface treatment, nitrogen-treated V_2O_5 provides a model to elucidate the connections between these physical properties. Figure 5f shows the adsorption spectra of V_2O_5 film electrodes before and after nitrogen treatment at $300\text{ }^\circ\text{C}$. The band gap narrowed from 2.37 to 2.28 eV , which is in agreement with the color of sample transitioning from light yellow to dark green (inset).^[184] Blue V^{4+} mixed with yellow V^{5+} obtains color green.

Beyond the atmospheric treatment and doping, surface coatings such as conductive polymers can also introduce gradient oxygen vacancies in V_2O_5 through in situ polymerization.^[185–188] The concentration of oxygen vacancies gradually decreases from the highest concentration at the surface, i.e., the interface between V_2O_5 and poly(3,4-ethylenedioxythiophene) (PEDOT), to near zero inside.^[186] During cycling, a local electric field develops, which is derived from lopsided charge distribution around oxygen vacancies. The vacancies induce a Coulombic driving force that promotes ionic transport, and the conductive PEDOT (or polyaniline or polypyrrole) coating synergistically enhances charge transfer kinetics by shortening the

charge transport distance.^[185,188] After long-term cycling, the oxygen vacancy concentration profile is redistributed as individual vacancies migrate inward under the applied voltage. The result is more V^{5+} are available for redox reactions and the specific capacitance increased.^[186] DFT calculations showed that migration of oxygen vacancies from the surface of V_2O_5 inward was thermodynamically favorable, as the Gibbs free energy of formation for vacancies was lower for the inner layers (-306.88 eV) of V_2O_5 than outer layers (-306.58 eV).^[187]

Surface defects introduced by atmospheric treatment and polymeric reduction are effective approaches to modify the surface chemistry of electrode materials. The increased surface energy and enhanced electrical conductivity promote the redox kinetics for energy storage. For further research, the feasibility of these strategies in SSE and the extension in ternary electrodes still need to be explored. In addition, whether the defect-rich surface causes accelerated rates of side reactions between the electrolyte and the electrode is another open question.

4.2. Artificial SEI and Coatings and the Space Charge Layer

Interface engineering using coatings has been widely employed to modify cathode, anode, and SSE materials in RBs. The main goals of interface engineering include: 1) preventing side reactions such as cation dissolution and surface passivation,^[189–192] 2) suppressing detrimental phase transitions, especially in layered cathodes,^[169,193,194] and 3) improving the wettability or compatibility among components.

Metallic anodes provide the lowest reference potential for a given battery system, and accordingly help enable high operating voltages for batteries. However, dendrite growth and surface passivation raise issues for battery safety and lifespan.^[191,195–200] Artificial layers with stable chemical compatibility and/or high mechanical strength are one path to address these issues, especially for enabling the success of Li metal anodes.^[201,202] Inspired by the SEI compositions produced during the battery formation process, artificial layers are introduced on the surface of Li metal before battery assembly. Based on the composition distribution, current artificial layers can be divided into two groups: i) single layer (Figure 6a) in which the composition is organic^[203,204] or inorganic^[205–208] or a mixture of both,^[209,210] ii) bi-layer (Figure 6b) which looks like the Janus configuration,^[202] where one layer intimately contacts the metallic anode and the other improves wettability with the electrolyte.^[152] Artificial layers can be implanted through in situ^[211,212] and ex situ^[208,213] methods. In the in situ method, additives are admixed in the electrolyte and the desired layer forms on the metal anode after battery cycling. For ex situ processes, the artificial layer is fabricated before battery assembly, which minimizes negative impacts on the electrolyte, but generally adds complexity to processing and manufacturing steps. The in situ method unavoidably consumes electrolyte, but the reaction order can be regulated by the choice of species that will be adsorbed in the inner Helmholtz plane (IHP). For example, NO_3^- has a lower energy barrier to pass the IHP and is preferentially adsorbed on Li surface. This helps prevent the reduction of TFSI⁻ (Figure 6c).^[214] Regardless of the configuration, a functional artificial layer requires high ionic

conductivity, strong mechanical strength, and high chemical stability. As one example, poly(dimethylsiloxane) films are mechanically and chemically stable and have been implanted to protect Li metal from side reactions. Symmetric Li//Li cells with this interlayer demonstrated a high Coulombic efficiency ($\approx 95\%$) in a conventional carbonate electrolyte after over 200 cycles at a current density of 0.5 mA cm^{-2} , and a LiFePO₄//Li full cell maintained a capacity of 140 mAh g^{-1} with a stable Coulombic efficiency of 99.8% after 100 cycles at 0.5 C.^[204] Li₃N has a high Li-ion conductivity of $\approx 10^{-3}$ S cm^{-1} at room temperature^[215] and is implanted onto Li metal anode by replacement of a Cu₃N pre-coating layer to reduce charge transfer resistance.^[213] In another iteration, a mixed ionic and electric conduction layer comprised of inorganic Li species (LiF, Li₃N, LiOH, Li₂O) and metallic Cu was generated to modify a Li metal anode.^[216] This layer possessed a Young's modulus of 12.9 GPa, exceeding the threshold of 6.0 GPa^[217] for inhibition of Li dendrite growth, and its ionic and electrical conductivities were around 10^{-2} and 10^{-4} S cm^{-1} , respectively.^[216] To screen for mechanically stable artificial layers, DFT calculations have been used to evaluate bi-layer artificial SEIs. A combination of graphene and LiF was found to exhibit the highest mechanical strength (Figure 6d) due to the stable interface derived from the anisotropic character and the defective structure.^[202] The high mechanical strength prohibits dendrite growth and high conductivities facilitate fast Li stripping and plating. Whether or not the mixed ionic and electronic conduction layer is effective at restraining the side reaction between Li metal anode and the nonaqueous electrolyte is a controversial issue because the continuous electron exchange between the electrolyte and electrode implies a continuous side reaction and consumption of the electrolyte.

In a magnesium system, fluorination has been shown to help overcome the issue of Mg passivation.^[218] In Figure 6d, when Mg ions are stripped from the surface of Mg foil, Cl⁻ from the electrolyte preferentially adsorbs on the fresh surface and the byproducts block Mg transport in the subsequent cycles. An ex situ chemically stable MgF₂ layer allowed for Mg transport and prevented passivating side reactions to enable relatively stable cycling for a Mg-ion battery.^[218] Other conductive fluoride layers, specifically amorphous LiF have been reported recently.^[206,219] It should be noted that how ions pass through these crystalline or amorphous inorganic layers has not been thoroughly investigated yet.

Cathodes easily undergo surface phase transitions, and the effects of cation dissolution and moisture are difficult to eliminate completely during industrial production. Trace water easily attacks PF₆⁻ in conventional electrolytes to produce hydrogen fluoride (HF), which will decompose spinel LiMn₂O₄ to release Mn²⁺ via disproportionation^[220] (Figure 7a). The dissolved Mn²⁺ can then redeposit on the LiMn₂O₄ surface or precipitate on the surface of the anode.^[221] At the same time, some impurities such as MnF₂ and Li-Mn-O compounds appear at the surface of LiMn₂O₄.^[189] Layered LiCoO₂ has a similar dilemma. When it is charged above 4.3 V, the phase transforms from O3 to O1 type, meaning the close-packed oxygen changes from ABCABC to ABAB stacking.^[222] If the cut-off voltage exceeds 4.5 V, it will cause Co²⁺ dissolution and oxygen release.^[136] Ternary cathodes such as Ni-rich, Li-rich, and Mn-rich oxides can be regarded as the derivatives of layered LiCoO₂, and some of its drawbacks are inherited.^[223–225] For example, the surface of

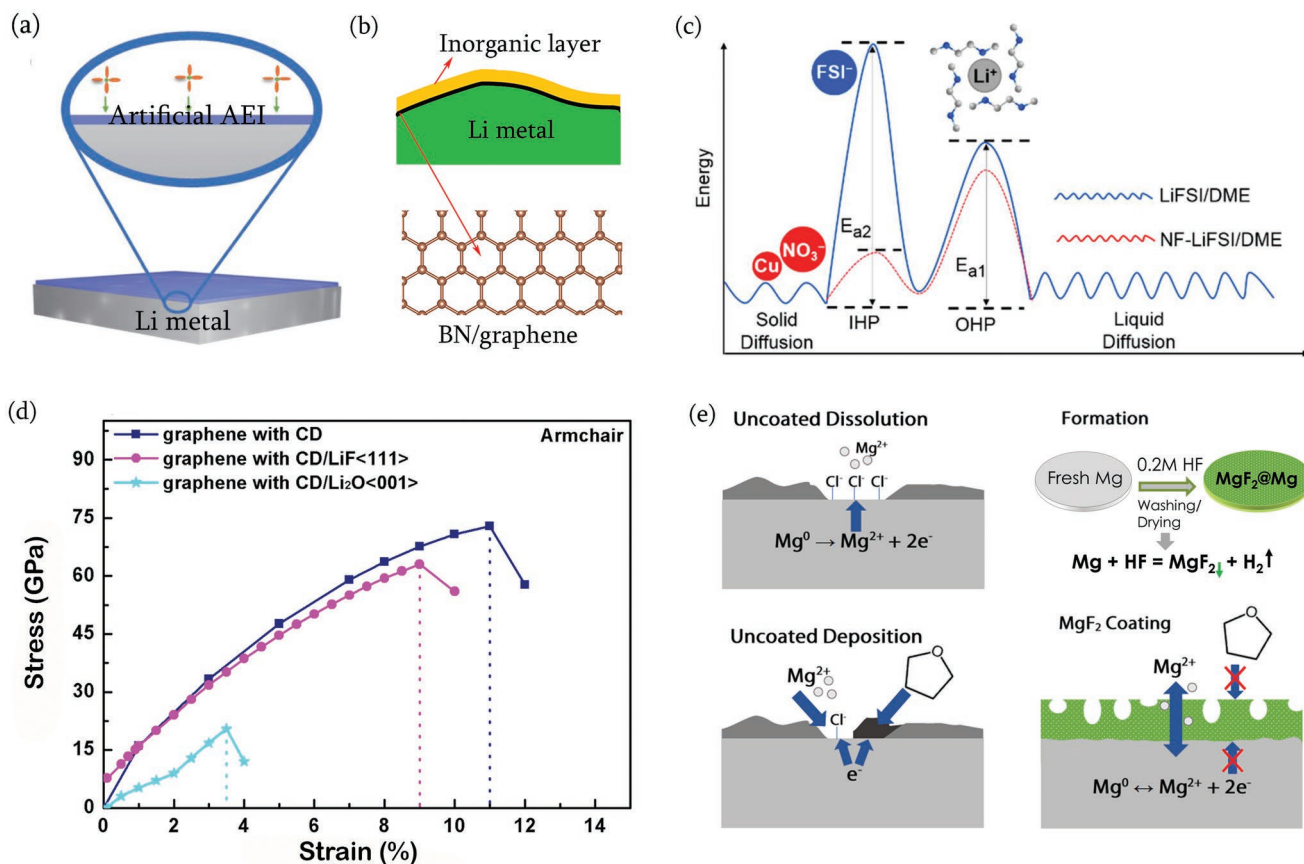


Figure 6. Schematic of artificial SEIs in a) single layer. Adapted with permission.^[210] Copyright 2017, AAAS, and b) bi-layer configuration. Adapted with permission.^[202] Copyright 2019, Elsevier. The main function of the artificial SEI is to prevent harmful side reactions. High mechanical strength is also important to suppress dendrite growth and penetration. c) Correlation between the energy barriers of Li-ion migration through the inner and outer Helmholtz planes, as influenced by both the anions and solvents in the electrolyte. Reproduced with permission.^[214] Copyright 2019, American Chemical Society. Controlling for the adsorbed species in the inner Helmholtz plane can influence the formation of SEI and protect against decomposition of the electrolyte. d) Calculated tensile stress–strain curves of graphene/LiF (111) and graphene/Li₂O (001). Reproduced with permission.^[202] Copyright 2019, Elsevier. Combining both effects of defects and anisotropy of different compositions provide a paradigm to design SEIs with high mechanical strength. e) Schematic of the formation and function of a fluorinated layer on a Mg metal anode. Adapted with permission.^[218] Copyright 2019, Elsevier. While most electrolytes produce passivating layers on metallic Mg anodes in nonaqueous Mg-ion batteries, the fluorinated layer not only exhibits chemical stability for preventing side reactions, but also allows for Mg-ion transport.

Li_xNi_{0.8}Co_{0.15}Al_{0.05}O₂ (NCA) is unstable, and local differences in ion diffusion kinetics cause an inhomogeneous state of charge within the NCA particle. The surface undergoes phase transitions from layered to spinel to rock-salt structure as more ions are removed near the surface. Electron energy loss (EEL) spectra exhibit the change of electron structure and bonding information (Figure 7b). When most of the Li ions are extracted, the electronic structure of the oxygen ions is strongly affected as reflected by the evolution of the oxygen K-edge peak from the EEL spectra.^[226] The peak associated with surface oxygen atoms shifts to higher energy since the more oxidized oxygen ions experience a greater effective nuclear charge from the transition metal cations and require more energy to excite the oxygen K-edge (i.e., 1s) electrons.^[227] The peak shift in the EEL spectra thus, demonstrates the change of local chemical surroundings of transition metal cations and the surface phase transition in the charging process of ternary cathodes based on the viewpoint of electronic structures.

Constructing an artificial layer, which protects the cathodes from HF attack or suppresses phase transitions could help improve the electrochemical stability. Oxides, phosphates, and fluorides are common choices because of their structural stability and compatibility with electrode materials.^[228–233] For examples, “AlPO₄” coating on LiCoO₂ can react with HF and trap the dissolvable Co²⁺ to form a stable inorganic layer that improves electrochemical stability.^[136] For a LiNi_{0.76}Mn_{0.14}Co_{0.10}O₂ cathode, liquid electrolyte penetrates along the grain boundaries of the secondary particles and forms SEI containing Li₂CO₃, LiF, and LiFPO_x. Coating grain boundaries of the secondary particles with Li₃PO₄ (LPO) (Figure 7c) not only provides a fast ion diffusion channel, but also eliminates intergranular cracking and the layered-to-spinel transformation.^[234] However, the poor electronic conductivity of phosphate and slight cation mixing at the outermost surface layer decrease the Li-ion diffusion kinetics and limit the rate capability. An extended study employed PEDOT as the conductive

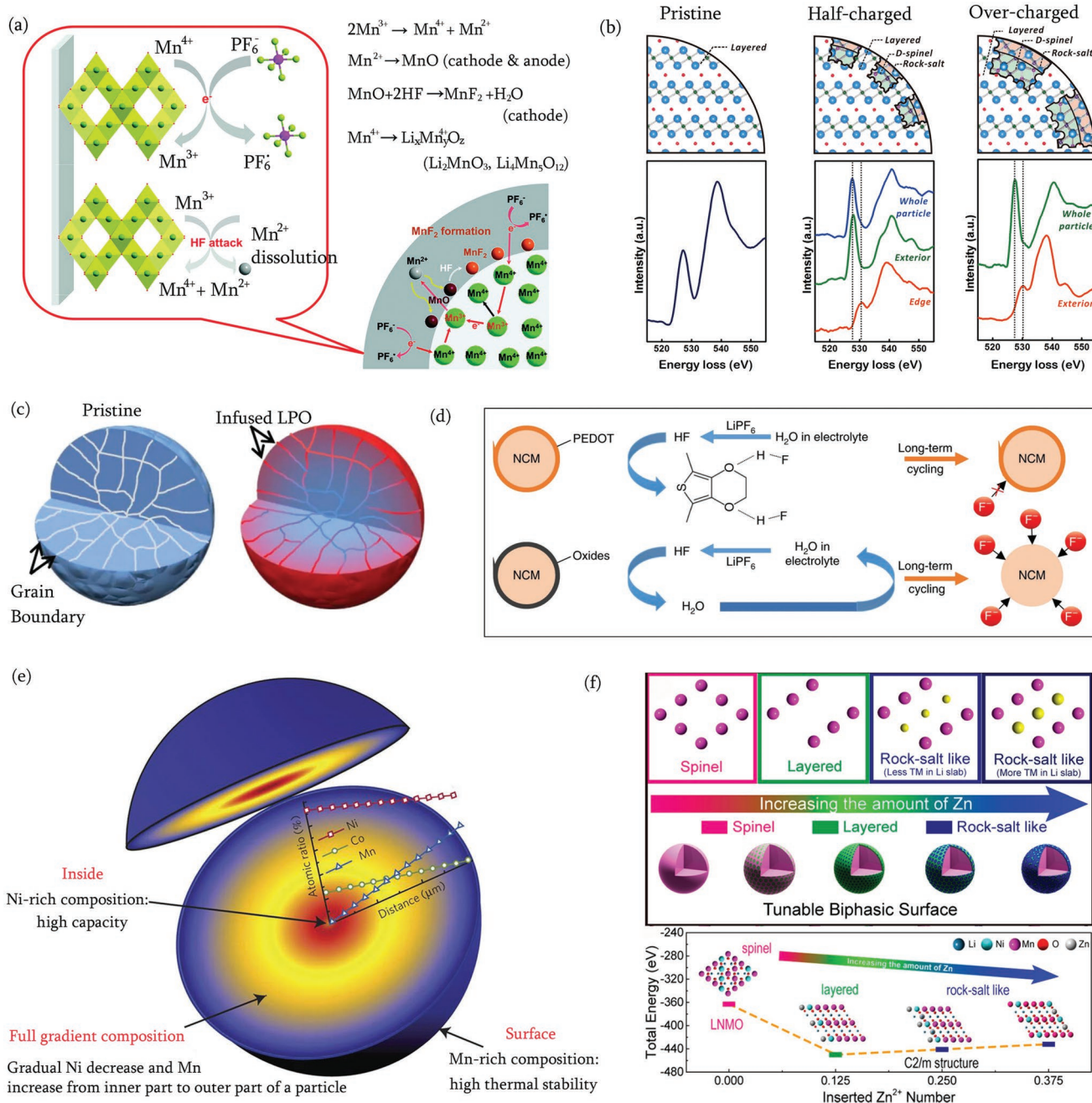


Figure 7. a) Schematic of Mn^{2+} dissolution and SEI formation on a LiMn_2O_4 cathode surface. Adapted with permission.^[66] Copyright 2013, American Chemical Society. b) Surface phase transition and the corresponding electronic structure evolution of the oxygen K-edge of $\text{Li}_x\text{Ni}_{0.8}\text{Co}_{0.15}\text{Al}_{0.05}\text{O}_2$ upon charging, as determined by EELS. Adapted with permission.^[226] Copyright 2014, American Chemical Society. Half- and over-charged are defined as $x = 0.5$ and 0.1 , respectively, in the chemical formula. c) Tailoring grain boundary by infusing LPO into the secondary particles. Adapted with permission.^[234] Copyright 2018, Springer Nature. d) Schematic illustration of the suppressing effect of PEDOT on HF attack to oxides, while the corrosion loop happens on the bare oxides. Reproduced with permission.^[235] Copyright 2019, Springer Nature. e) Schematic of the concentration gradient in NCM cathode with a Mn-rich surface and Ni-rich core. Adapted with permission.^[236] Copyright 2012, Springer Nature. The aim is to maximize the high capacity from Ni-rich core and the highly thermal stability from Mn-rich shell. f) Surface-phase evolution of $\text{LiNi}_{0.5}\text{Mn}_{1.5}\text{O}_4$ with the increase of Zn content. Reproduced with permission.^[238] Copyright 2019, American Chemical Society. The amount of Zn in the surface layer could be tuned to produce mostly a layered phase or predominantly a rock-salt-like surface.

skin to mitigate phase transformations and intergranular and intragranular mechanical cracking.^[235] The dioxane ring in PEDOT structure can coordinate with HF by forming O—H—F

covalent bonds, which alleviate transition metal dissolution from the surface attack by HF from the electrolyte (Figure 7d). Meanwhile the PEDOT skin acts as an isolation layer to prevent

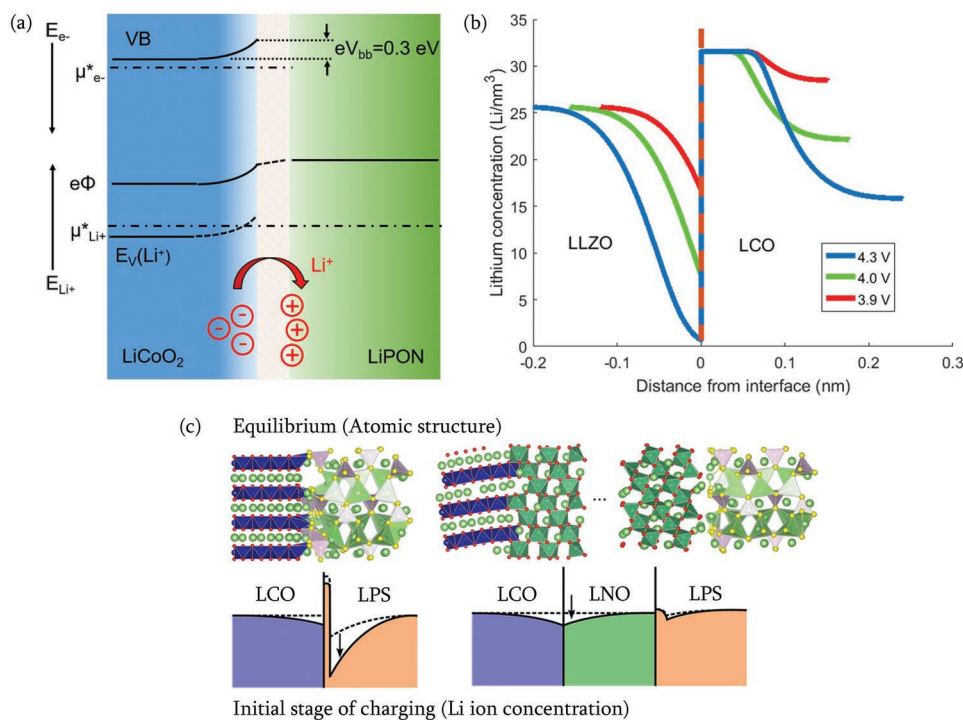


Figure 8. a) Schematic of the electrochemical potentials at the LiCoO_2 – LiPON interface. eV_{bb} : bending of the VB, Φ : the inner electric potential profile, $\mu_{e^-}^*$: the Li-ion electrochemical potential. Reproduced with permission.^[239] Copyright 2017, American Chemical Society. b) Lithium-ion concentration at the $\text{Li}_7\text{La}_3\text{Zr}_2\text{O}_{12}$ – LiCoO_2 interface at voltages of LiCoO_2 , 4.3 V = $\text{Li}_{0.5}\text{CoO}_2$, 4.0 V = $\text{Li}_{0.7}\text{CoO}_2$, and 3.9 V = $\text{Li}_{0.9}\text{CoO}_2$. Reproduced with permission.^[243] Copyright 2018, American Chemical Society. The thickness of space charge region is less than 1 nm, thus the resistance effect can be ignored. c) Illustration of the Li-ion concentration at the interfaces of $\text{LiCoO}_2/\beta\text{-Li}_3\text{PS}_4$ and $\text{LiCoO}_2/\text{LiNbO}_3/\beta\text{-Li}_3\text{PS}_4$. Reproduced with permission.^[245] Copyright 2014, American Chemical Society. The buffering layer eliminates ion accumulation at the interface and decreases the interfacial impedance.

the direct contact of the flammable electrolyte from the surface of the ternary cathodes, and the suppressed oxygen release at higher voltages. This mitigates the buildup of internal pressure that is one of the primary driving forces for the intragranular cracking. The distinct advantage of PEDOT is the high electronic conductivity and Li-ion permeability in comparison with the infused Li_3PO_4 ,^[234] resulting in a lower impedance in the battery. Beyond the artificial layers, gradient elemental distribution on the particle surface has been proposed. Figure 7e shows the early-stage concept to utilize the high capacity of the Ni-rich core and the thermal stability of the Mn-shell to maximize the electrochemical performance of a ternary $\text{LiNi}_{0.75}\text{Co}_{0.10}\text{Mn}_{0.15}\text{O}_2$ (NCM) system.^[236] The scalability of this concept remains to be seen, but it motivates the use of surface gradient doping to overcome challenges in this area.^[237,238] As a final example, annealing a ZnO coating on $\text{LiNi}_{0.5}\text{Mn}_{1.5}\text{O}_4$ induces the surface phase transition from spinel to layered and then rock-salt-like phase. The character of the surface could be tailored by adjusting the thickness of the ZnO layer, where the rock-salt phase dominated the surface as that Zn content increased (Figure 7f). This provided a way to tune the biphasic surface since the layered structure provides greater electrochemical stability while the rock-salt phase provides greater structural stability.^[238]

Similar to ion transport and electron exchange at solid–liquid interfaces, solid–solid interfaces in SSB are always accompanied with interphases formed during the fabrication process. The functional solid–solid interface should be energetically stable to minimize the growth of the reaction layer,^[239] which depends

on the chemical potentials of ions and electrons between the contacted SSE and electrode. Electrons and ions hosted in a material are associated with corresponding defects at a given chemical potential. Chemical potential also can be described by energy levels, such as electron states, ion site energy, and their respective concentrations. Interfacial impedance and stability are related to these energy levels and the corresponding concentration of electrons and ions.^[240] During cycling, ions and electrons move across the interface, which induces carrier redistribution and the formation of a double layer.^[240] At the solid–solid interface, equilibrium specifically refers to that of Li ions.^[241] The electrons and other ionic species stay at a nonequilibrium state at the interface, causing the growth of the reactive interlayer. At the LiCoO_2 – LiPON interface (Figure 8a), a chemical potential difference of 0.3 V appears, which originates from the equilibration of Li ions at the interface. Upon charging, LiCoO_2 loses Li ions and forms negatively charged Li-vacancies (V_{Li}^-), and the inserted Li ions in LiPON produce positively charged Li-interstitials (Li_i^+). Both species accumulate at the interface on their respective side to form the space charge layer. Its thickness depends on their carrier concentration. It is reported that LiPON has a high Li-ion concentration of around $1.5 \times 10^{20} \text{ cm}^{-3}$,^[242] thus the space charge region becomes very narrow. V_{Li}^- accumulation at the interface can cause band bending and the formation of oxygen vacancies.^[239] The chemical potential difference drives oxygen ion migration to the LiPON side and combine with Li ions. This process induces the formation of reaction interlayer that increases the

interfacial impedance. In $\text{Li}_7\text{La}_3\text{Zr}_2\text{O}_{12}$ – LiCoO_2 system, the space charge region is about 0.25 nm at 4.3 V, which is twice the thickness at 3.9 V. The Li ion concentration near the LLZO is decreased by 35% and 95%, at 3.9 and 4.3 V, respectively. Since the thickness of the space charge region is less than 1 nm, its contribution to Li ion transport resistance is negligible.^[243] Analogous to the situation in conventional liquid-electrolyte battery interfaces, inserting a buffering layer between the SSE and the cathode can eliminate the ion accumulation at the interface and decrease interfacial impedance. In one iteration, an ionically conductive LiNbO_3 coating (ionic conductivity of $\approx 10^{-5} \text{ S cm}^{-1}$ ^[244]) was used as the buffering layer between LiCoO_2 and $\beta\text{-Li}_3\text{PS}_4$.^[245] The Li-ion concentration across the two interface is shown in Figure 8c. Li ions accumulate at the ridge oxygen anions of CoO_6 octahedra, resulting in a deformed space charge layer. At the same time, Li ion in $\beta\text{-Li}_3\text{PS}_4$ is driven to the interface upon charging, which grows the space charge region and increases the interfacial impedance. LiNbO_3 buffers the ion accumulation at the interfaces and eliminates the growth of the reaction layer.^[245]

There are many process modifications that can be employed to control defects and engineer new interphase layers in SSBs. However, the new solid–solid interface adds new considerations for SSB design because it gives rise to reaction and space charge layers. The determinants of the thickness of space charge region require more investigation in order to realize SSEs with lower interfacial resistance.

5. Interfaces of Oxide Conduction Layer/Halide Perovskite of PSC

Just like RBs, surface and interface properties determine power conversion performance in PSCs. PSCs convert photoenergy to electricity through very different optoelectronic processes in comparison with conventional solar cells such as quantum dot (QD) or dye-sensitized solar cells (DSCs). PSCs absorb photons and generate excitons in perovskite layers before separating and transporting electrons and holes at the interfaces to the HTL or ETL.^[246,247] So in addition to optimizing the chemical composition, electronic structure, crystallinity, and microstructure, PSC must also be minimized charge recombination at these interfaces.^[248,249]

To achieve high-efficiency PSCs, several criteria must be met for the bottom or top carrier transport layers: a) high transmittance to avoid superfluous energy loss, b) well-matched energy levels for efficient charge transfer, and hole or electron blocking, c) high carrier mobility and extraction ability, d) long-term stability.^[250] An optimized interface of oxide conduction layers could adjust their band energy level to match perovskite better or enhance their ability of charge extraction from perovskite.

Titanium dioxide (TiO_2) is the earliest electron transfer material used in perovskite devices as part of the technical revolution moving from DSCs to halide perovskite film solar cells.^[9] Due to the high stability and CB level, TiO_2 is widely used as the ETL for PSCs, including planar and mesoporous structural solar cells. However, two intrinsic disadvantages hinder its development in PSCs. One is the low electron mobility, which is only $< 1 \text{ cm}^2 \text{ V}^{-1} \text{ s}^{-1}$ for the bulk film.^[250] The charge cannot be extracted in a timely manner, which causes charge

accumulation and recombination at the interface and induces hysteresis.^[251] Another disadvantage is that the sensitization of TiO_2 promotes decomposition of the perovskite when exposed to ultraviolet light.^[252]

One way to solve the charge accumulation and hysteresis problems of TiO_2 is to add a mesoporous layer on the compact nanocrystalline layer. Increasing the contact area between perovskite and TiO_2 leads to more transmission channels of carriers, which reduces the hysteresis.^[253,254] Unfortunately, this does not fully overcome the challenges. As another pathway, elemental doping in TiO_2 was demonstrated to enhance electron mobility. In one instance, mesoporous TiO_2 was n-doped through a lithium salt surface treatment, inducing a partial reduction of Ti^{4+} to Ti^{3+} and passivating electronic defect states which act as nonradiative recombination centers.^[255] The halide salts not only passivate the surface of TiO_2 but also improve the wettability between TiO_2 and perovskite. In another iteration, when TiO_2 surface was modified with CsI and CsBr. One side, Cs^+ ions could reduce the formation energy of perovskite and purify the phase composition.^[256] The other side, halide ions could passivate the surface defect of perovskite,^[13] resulting in a high fill factor (FF) of $\approx 80\%$, an open circuit voltage (V_{OC}) of 1.14 V, and a PCE up to 21% with negligible hysteresis.^[257] In addition, the introduction of chlorine capping in compact TiO_2 reduces the trap states, leading to the high PCE.^[12]

Adding an interlayer with high electron mobility is another approach to accelerate the charge extraction and improve the stability^[12] against the ultraviolet light. A fullerene self-assembled monolayer (C_{60}SAM) applied to mesoporous TiO_2 enhances electronic coupling between perovskites and polymer semiconductors and reduces recombination.^[258] Another common technique uses very thin layers of polymethyl methacrylate (PMMA):phenyl- C_{61} -butyric acid methyl ester (PCBM) mixtures to suppress charge recombination at the perovskite/mesoporous- TiO_2 interface and the cross-section scanning electron microscopy (SEM) can be seen in **Figure 9a**.^[259] The incorporation of nonconducting PMMA and conductive n-type PCBM co-passivates the interface without increasing the series resistance. As shown in **Figure 9b**, passivation clearly increases the V_{OC} while **Figure 9c** shows that the carrier lifetime is prolonged by reducing trap states. The device performance is improved accordingly, as V_{OC} increases from 1.09 to 1.16 V and PCE from 19.6% to 20.4%. Lastly, the I – V curves recorded at different scanning rates prove that the hysteresis is suppressed by mixture passivation.^[259]

In addition to surface modification, using different phases of TiO_2 and dopants have been adopted to improve the performance of PSCs with TiO_2 as the ETL. In one report, a rutile TiO_2 ETL enhances the extraction of electrons and increases the charge collection efficiency of the solar cells.^[260] Another recent work introduced a rutile TiO_2 layer between FTO (fluorine-doped tin oxide) and anatase TiO_2 layer, resulting in a bilayer ETL. This junction ETL strategy yields several benefits, including excellent carrier extraction, defect passivation, and reduced recombination at the ETL/perovskite interface.^[261] As one example using dopants, yttrium-doped TiO_2 (Y-TiO_2) was used as the ETL to enhance electron extraction and transport. The Fermi level in the Y-TiO_2 exhibits a slight upward shift, indicating an increased donor concentration with the enhanced conductivity.^[262]

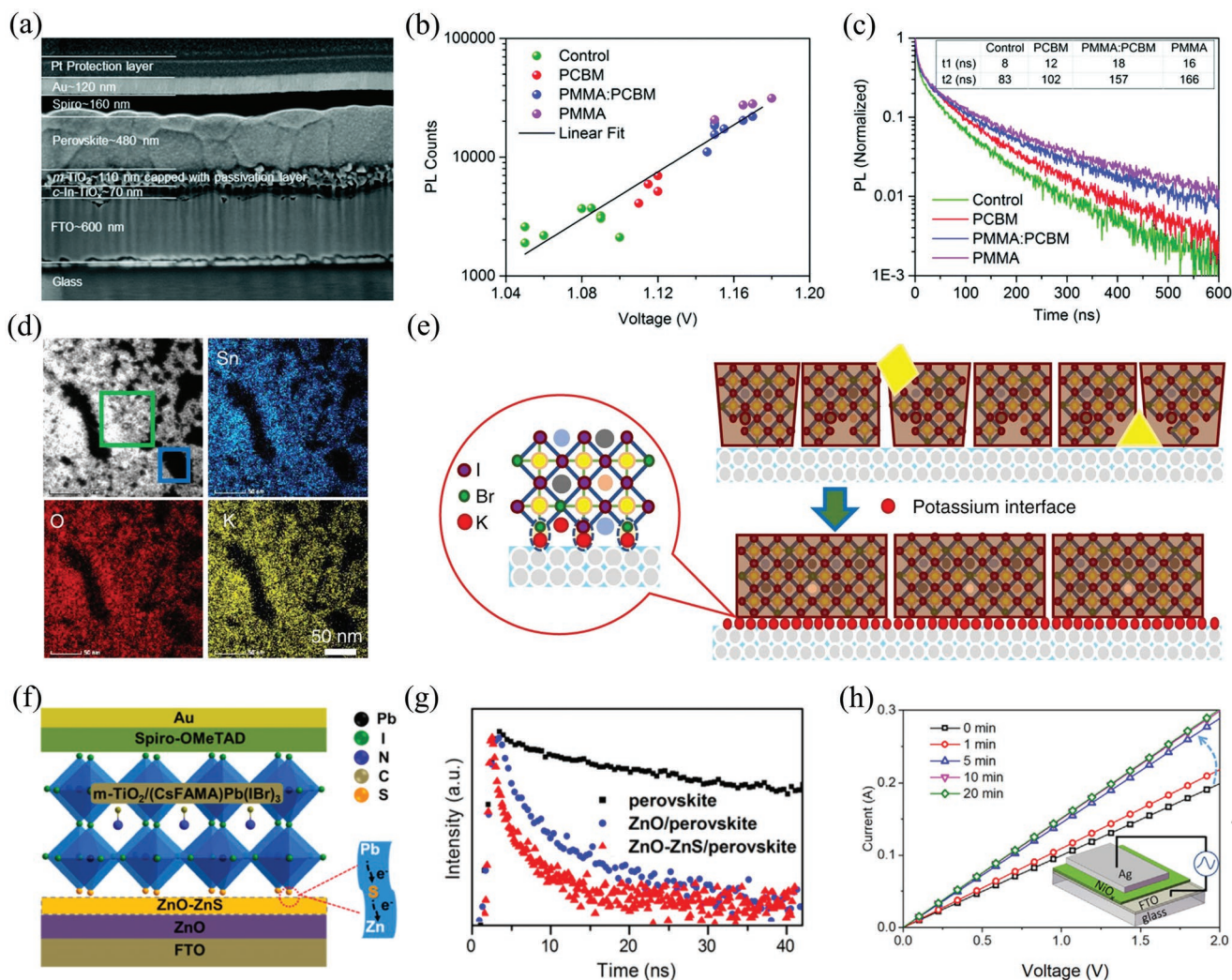


Figure 9. a) SEM cross-section of a PSC. b) Logarithmic plot of PL intensity. c) TRPL decay measurements. Reproduced with permission.^[259] Copyright 2017, Royal Society of Chemistry. d) STEM-EDX images of Alfa-SnO₂. e) A schematic of the perovskite growth process on different substrates. Reproduced with permission.^[263] Copyright 2018, Springer Nature. f) Structural characterization of ZnO-ZnS ETL-based device. g) TRPL spectra. Reproduced with permission.^[264] Copyright 2019, American Chemical Society. h) I-V curves for FTO/NiO_x/Ag structures where NiO_x films have different UVO exposure times. Reproduced with permission.^[265] Copyright 2019, Wiley-VCH.

Tin dioxide (SnO₂) became one of the most popular electron transport materials for PSCs because of its many beneficial properties, including the high electron mobility (240 cm² V⁻¹ s⁻¹), excellent chemical and photocatalytic stability, suitable CB level, and low-temperature processability.^[250,266] Moreover, the commercial SnO₂ nanocrystal solutions (e.g., from Alfa Aesar) can be used directly to fabricate the ETL for high-efficiency PSCs. Thus, the device fabrication process is greatly simplified by low-temperature annealing (150 °C) and a facile deposition method with commercially available products.^[251]

However, SnO₂ nanoparticles present two drawbacks including the large number of surface defects and low wettability. Surface modification of SnO₂ has achieved satisfactory results.^[267–269] Among the approaches, UV-ozone (UVO) treatment can remove surface contaminants and improve surface wettability.^[270] For example, the PCE of the devices was enhanced to 18.03% with Sol/UVO-ETL technology.^[271] Another

approach is to improve the wettability and manipulate energy level alignment between SnO₂ and perovskite. A C₆₀ interlayer was introduced prior to depositing perovskite, resulting in less charge recombination and longer carrier lifetime.^[272] The C₆₀-containing self-assembled monolayer (C₆₀-SAM) enhances the electron coupling between the SnO₂ and perovskite layers, leading to the low trap density and less ion migration.^[273] By C₆₀-SAM passivation of SnO₂, the maximum PCE is increased to 19.03%.^[274] Similar to TiO₂ as described above, the introduction of PCBM as a passivation layer between SnO₂ and perovskite led to a PCE of 19.12% with high V_{OC} of 1.12 V, attributing to enhanced electron transmission and reduced charge recombination.^[269] Graphene was also adopted to improve the conductivity of SnO₂ and passivate surface defects of SnO₂. PSC fabricated with graphene QDs (GQDs) added to the spin-coating precursor solution (SnCl₂·2H₂O) could achieve a high steady-state PCE of 20.23% with very little hysteresis.^[275]

Halide salts, such as KCl, were also shown to passivate the ionic surface defects which usually cause detrimental carrier recombination. Defect passivation significantly suppresses the recombination at the SnO₂/perovskite interface, resulting in a high V_{OC} of 1.151 V and PCE of 20.5%.^[268]

To enhance the electronic property of nanocrystalline SnO₂, the elemental doping has been shown to enhance the carrier mobility in SnO₂ and influence the energy levels in devices. For example, a small amount of Sb doped in SnO₂ nanocrystals would result in the enhanced electrical conductivity, and the V_{OC} increased because of the Fermi level of the ETL rose.^[276] With Mg doping, a SnO₂ film is demonstrated to increase electron mobility. However, this strategy also lowers the CB level so as to reduce the offset energy between the doped ETL and perovskite layers. As a consequence, the V_{OC} is reduced. Nevertheless, the device's PCE is increased by the improvement of interfacial contact, higher electron mobility, and suppression of carrier recombination.^[277] Analogously, yttrium-doped tin dioxide (Y-SnO₂) synthesized by an in situ hydrothermal growth process at 95 °C, promotes the formation of SnO₂ with a more homogenous distribution. This means ETL intimately connects with the perovskite layer to improve electron transfer. Furthermore, the energy level of the ETL is better aligned with the perovskite because the band energy levels are shifted up, resulting in less charge recombination at the interface.^[278]

The addition of the stabilizer KOH in the colloidal precursor solution was found to be one important factor for enhancing the performance of the solar cells.^[263] As shown in Figure 9d, the detected K element in scanning transmission electron microscope–energy dispersive X-ray (STEM–EDX) images of α-SnO₂ colloidal provides an evidence to support the argument about the K influence on the performances of cells. In previous reports, K⁺ can combine with Br from perovskite to form KBr at the surfaces and grain boundaries, which immobilizes the surplus mobile halide ions and vacancies.^[279,280] To emphasize the effect of KOH, the deionized water bath was employed to remove the KOH. The performances of devices based on α-SnO₂, water α-SnO₂ (using deionized water-bath to remove the residual potassium ions on FTO), and KOH-treated water α-SnO₂ are tested. The water α-SnO₂ devices show serious hysteresis, while after KOH treating the water α-SnO₂, the hysteresis disappeared, indicating that KOH is the critical factor to enhance the property of devices. It was speculated that K⁺ improves the crystallization of the perovskite and passivates defects by forming KBr to pad grain boundaries, as shown in Figure 9e.^[263] Introduction of ethylene diamine tetraacetic acid (EDTA) to α-SnO₂ was found to form EDTA-complexed SnO₂. The PSC fabricated with EDTA-complexed SnO₂ as the ETL attains a PCE as high as 21.60%. EDTA decreases the Gibbs free energy for heterogeneous nucleation of the perovskite, which produces a higher quality film. The treatment also increases the electron mobility of the SnO₂ ETL because the lone-pair electrons of EDTA can be interacted with the vacant d-orbital of the transition metal atom, which positively affects PCE and long-term stability of the device, respectively.^[281]

Zinc oxide (ZnO) is another promising material for PSC ETLs. The electron transportation mobility of bulk ZnO can reach as high as 205–300 cm² V⁻¹ s⁻¹ due to the self-compensation effect^[250] and its CB energy is –4.2 eV.^[282] Unfortunately, the side photochemical reactions between ZnO and halide perovskites inhibit its

application. This similar problem was also demonstrated in the DSCs. The surface modification of ZnO photoanodes has been recognized as an indispensable approach to improving the performance of DSCs,^[283,284] and is equally suitable for PSCs.

The recent works have obtained decent achievements via the surface modification of ZnO or insertion of an interlayer between ZnO and perovskite layers. For example, ZnO layer was coated with 3-aminopropanoic acid (C₃-SAM), which not only effectively reduces the trap states but also improves the morphology of CH₃NH₃PbI₃ perovskite crystals.^[285] The interfacial energy level alignment between ZnO and perovskite layers is also improved due to the permanent dipole moment of C₃-SAM.^[285] Similar work reported a monolayer of graphene at the interface of the ZnO and perovskite layers, which enhances both the carrier extraction of ZnO and the thermal stability of the devices. Another organic material, 3-(pentafluorophenyl)propionamide, was spin-coated on the ZnO ETL to passivate surface traps, resulting in a PCE of 21% and an enhanced device stability.^[286] Up to now, placing organic polymer interlayers between the ZnO and perovskite layers has been the most effective solution for improving the performance of PSCs. We think the interlayer may avoid the contact of ZnO and perovskite, meanwhile, it does not affect the electron extraction property. This idea maybe useful and helpful to other ETL materials.

In addition to organic interlayers, oxides have been employed to passivate ZnO layer. For example, ZnO nanorods coated with TiO₂ by a wet-chemical method demonstrated that both the efficiency and device stability were significantly improved.^[287] In another report, a thin MgO layer was introduced to passivate the surface of ZnO, which inhibits interfacial charge recombination.^[288] Moreover, the protonated-stabilizer ethanolamine (EA) further promotes the electron extraction performance of ZnO layer. The best performing efficiency of PSCs fabricated with the modified ZnO ETLs reaches PCEs of 21.1%.^[288] Zn₂SnO₄ (ZTO) as a third example was deposited in situ on ZnO nanocone as a protection layer to enhance the charge extraction ability of ZnO and improve the thermal stability of the device.^[289] To date, the performance of PSCs based on ZnO as the ETL still lags behind that of PSCs with TiO₂ and SnO₂ ETLs.

Recently, the novel fabrication of ZnO ETLs and dual-function ETLs was developed for PSCs, respectively. One effective approach is developed to obtain ZnO ETL with the combustion synthesis method.^[290] The combustion synthesis produced high-quality ZnO films with high crystallinity and low carbon contamination and no organic ligand residues, which overcomes the deficiencies of conventional sol–gel-processed ZnO ETLs. As a result, the corresponding PSCs exhibited PCEs approached 20%, which is the highest efficiency reported to date for a PSC with ZnO as the ETL.^[290] Surface ZnO has also been converted in situ into ZnS at the ZnO/perovskite interface by sulfidation to form a dual-function ETL, as shown in Figure 9f.^[264] The Pb²⁺ could be strongly bound with the S²⁻ from ZnS, which also passivates the halide vacancy traps in perovskite. This would passivate both the ZnO surface defects and perovskite halide vacancy traps, resulting in better electron extraction and less interfacial recombination. The photoluminescence (PL) spectra in Figure 9g shows improved electron transport across the ZnS and perovskite interface. Meanwhile, the deprotonation of protonated organic amine in perovskite is

also avoided by ZnS as the isolated layer. These features collectively lead to superb device efficiency and stability.^[264]

For p-i-n type PSCs (or inverted PSCs), nickel oxide (NiO_x) is widely used as the hole transport material on the bottom layer because it has good transmittance in the visible, and its VB edge level (5.2–5.4 eV) is well-matched to the perovskite VB (≈5.4 eV).^[291] In addition, its resistance to moisture, heat, and light, and minimal hysteresis make it one of the most promising inorganic HTLs for the inverted PSCs.^[291,292] Similar to the other oxide conductive layers, the high trap state of NiO_x causes charge recombination at the NiO_x and perovskite interface. As one approach to solve this problem, the surface of NiO nanocrystal layers was modified with diethanolamine (DEA). The –OH and amine groups from EDA could interact with Pb-based compounds. Thus, the perovskite crystallization and interfacial contact are improved due to the favorable dipole layer formed by the molecular adsorption, resulting in the enhancement of hole extraction/transport and thus the photovoltaic performance.^[293]

UVO treatment is usually used to clean conductive oxide substrate surfaces (e.g., indium tin oxide and FTO). Recently, the UVO has also been employed to treat ultrathin mesoporous NiO_x film.^[265] The electrical conductivity of the NiO_x film is proportional to the tangent of the *I*–*V* curve in Figure 9h, and is improved with the UVO treatment. The valance band maximum moves lower after UVO treatment, indicating better hole extraction. The perovskite grain size is also increased, which facilitates the transport and collection of photogenerated carriers because there are fewer grain boundaries.^[265] Moreover, the trap density is also reduced both in perovskite films and in devices. The performance of devices based on UVO-treated NiO_x exhibits a high PCE of 19.67%.^[265]

Another problem for NiO_x is its poor electrical conductivity. Many works have focused on metal ion doping into NiO_x to enhance the conductivity and further improve the interface between the perovskite and NiO_x layer. For this purpose, copper-doped NiO_x (Cu:NiO_x) presents an enhanced electrical conductivity of $8.4 \times 10^{-4} \text{ S cm}^{-1}$ that is much higher than $2.2 \times 10^{-6} \text{ S cm}^{-1}$ of pristine NiO_x.^[294] The corresponding inverted PSCs show 15.6% of PCE. As a further improvement, a low-temperature combustion method was developed to synthesize Cu-doped NiO_x.^[295] The crystallinity of Cu-doped NiO_x is clearly improved by this method, leading to even higher efficiency of 17.8%.^[295] Other dopants have included alkali metal cations. For example, using lithium-doped NiO_x (LiNiO) for the HTL helps to form a more stable tetragonal phase halide perovskite compared to that formed with more conventional PEDOT:PSS (polystyrene sulfonate) as the HTL. First-principles computational modeling also suggests good energy level matching between tetragonal MAPbI₃ and LiNiO. The enhanced performance of the solar cells based on the LiNiO layer is found to be directly related to the interface energy level alignment and sup-

pressed recombination at the HTL/perovskite interface. This is attributed to the high crystallinity of the perovskite thin film and clean LiNiO interface.^[296] Cesium cation is also used as an A-site dopant of the perovskite (ABX₃ structure) to improve structural stability.^[256] Recently, cesium-doped NiO_x has been studied to explore the impact of Cs on the optoelectronic properties of NiO_x and the photovoltaic performance of the solar cells. The device displays a high PCE of 19.35%, which is mainly attributed to the significant improvement in hole extraction and better band alignment between the HTL and perovskite.^[297]

6. Surface Passivation of Perovskite Layer for PSCs

Because the surface of the perovskite layer is formed by the termination of crystallization and growth, there is an abundance of ionic vacancies and dangling bonds on the perovskite crystal surface, resulting in the much more defects and high trap density.^[45] However, these defects tend to be inert and do not necessarily lead to recombination. First-principles calculations' results have been helped explain the origin of perovskite materials' tolerance for defects.^[45,46] These halide perovskite defects are divided into two categories depending on how detrimental their carrier-trapping ability is. One category of defects has shallow energy levels (shallow defects). The defects have little effect on the transport of the charge carriers. MA vacancy (V_{MA}^{\cdot}), MA interstitials (I_{MA}^{\cdot}), and Pb²⁺ interstitials (I_{Pb}^{\cdot}) are examples of shallow defects (Figure 10).^[46] In contrast, deep defects can trap charge carriers during the extraction and transfer process. Fortunately, due to the high formation energy, few of these defects could appear in the perovskite layer. On the basis of previous reports, I[−] vacancy (V_I^{\cdot}), PbI₂ interstitials ($I_{PbI_2}^{\cdot}$), I⁰ interstitials (I_i^0), etc., were generally accepted as the deep defects.^[13,46,298]

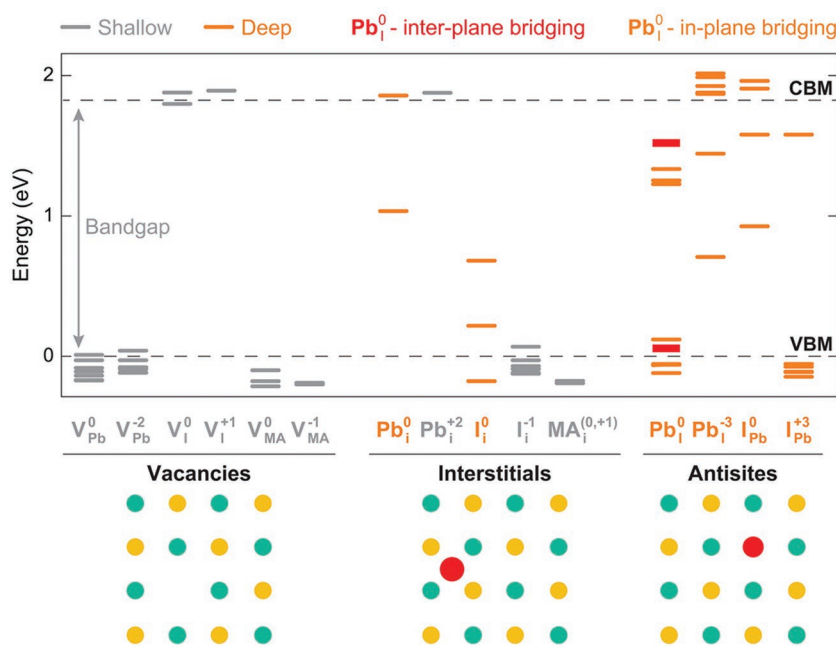


Figure 10. Energy levels associated with the defect states corresponding to neutral and charged vacancies, neutral and charged interstitials, and neutral and charged states associated with antisites (Pb_i and I_{Pb}). Reproduced with permission.^[46] Copyright 2014, American Chemical Society.

Surface passivation has been considered as the key process to reduce the deep defects and improve the charge collection efficiency of PSCs. Many strategies have been investigated to passivate these defects and achieve excellent results. Here, we will discuss the surface passivation of two types of halide perovskites, the organic–inorganic hybrid and all-inorganic perovskites.

6.1. Organic–Inorganic Halide Perovskite Devices

6.1.1. Halide Salts

Halide vacancies (e.g., I^- vacancy) belong to deep defects and thus many halide salts are introduced to passivate these vacancies. Halide salt components are usually introduced as passivating materials. For example, the quaternary ammonium halides were employed to passivate the surface ionic defects, leading to longer carrier lifetime.^[299] Supported by DFT calculations, several different types of hybrid perovskite ionic defects are efficiently reduced, leading to a high PCE of 21%.^[299] In this model, 1,8-octanediammonium iodide combines with residual PbI_2 on the surface of perovskite film and forms a 2D structure. The V_{OC} of the device increases from 1.04 to 1.13 V with this defect-passivating component, indicating the suppression of charge recombination.^[300] The ambient stability of PSC is also significantly improved by the 2D structural surface layer of perovskite.^[300]

The post-treatment of perovskite layer is a simple and efficient surface passivation method. Self-assembling post-treatment with *tert*-butylammonium iodide (tBAI) for the perovskite surface was introduced to passivate surface and grain boundary defects.^[301] The large-sized tBA cation is incorporated into the perovskite crystal structure, improving the structural stability of perovskite.^[301] Similarly, phenethylammonium iodide (PEAI) can form on the perovskite surface

and suppresses nonradiative recombination without any annealing process, as shown in Figure 11a.^[302] The iodine vacancies on the surface are modified by I^- ions of PEAI, as shown in Figure 11b. Furthermore, annealing is not shown to be beneficial in this process, since it forms a 2D structural layer of PEA_2PbI_4 that is not as effective as pure PEAI. X-ray diffraction (XRD) patterns show that with the annealing temperature increasing, the intensity of PEAI peak decreases while PEA_2PbI_4 peak intensity gets stronger, which corresponds to shorter carrier lifetime. Finally, an impressive PCE of 23.3% was authenticated with high J_{SC} of 25.2 mA cm^{-2} , V_{OC} of 1.18 V, and FF of 78.4%.^[302] A facile and effective method with FAI was introduced to passivate I^- vacancies (Figure 11c).^[303] The time-resolved PL (TRPL) curves obtained by measuring light exiting from the glass side and surface side overlap together after FAI passivation.^[303] After passivation, the two TRPL curves overlap together, demonstrating fewer surface defects on the perovskite, indicating that FAI is introduced to passivate $MAPbI_3$ film and results in a longer carrier lifetime.^[304] A solution-processed secondary growth technique was used to form a more n-type perovskite thin layer on the top region of the perovskite film.^[305] The n-type perovskite thin layer could occupy the vacant traps and reduce the rate of trap-assisted recombination, achieving a high PCE greater than 21% and stabilize PCE of 20.91%.^[305] Excess PbI_2 on the surface of perovskite often serves as a passivation layer and PbI_2 content was systematically investigated to study its effect on device performance.^[306] A moderate amount of residual of PbI_2 delivers stable and high-efficiency solar cell devices. Subsequently, double-side-passivated PSCs are constructed by intentionally distributing PbI_2 to both the front and rear surfaces and grain boundaries, resulting in the decrease of defect states at the interfaces of PSC device. So far, to obtain high-performance PSC devices, the excess PbI_2 is necessary (currently 10%).^[307]

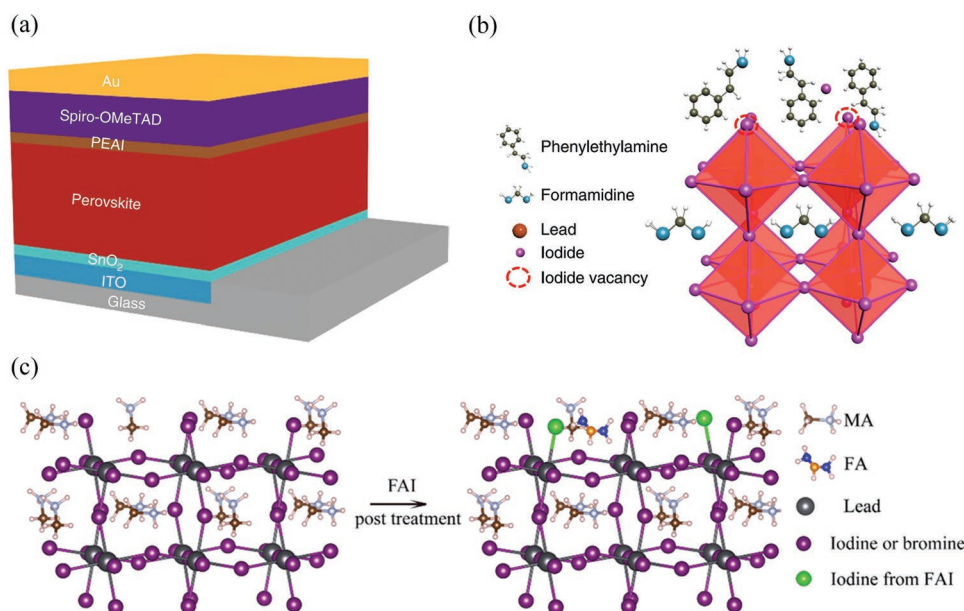


Figure 11. a) The device structure of the structure. b) Possible passivation mechanism of the PEAI layer for the perovskite film. Reproduced with permission.^[302] Copyright 2019, Springer Nature. c) Schematic illustration of the filling of I^- and MA^+ vacancies in the perovskite films by the FAI posttreatment process. Reproduced with permission.^[303] Copyright 2018, American Chemical Society.

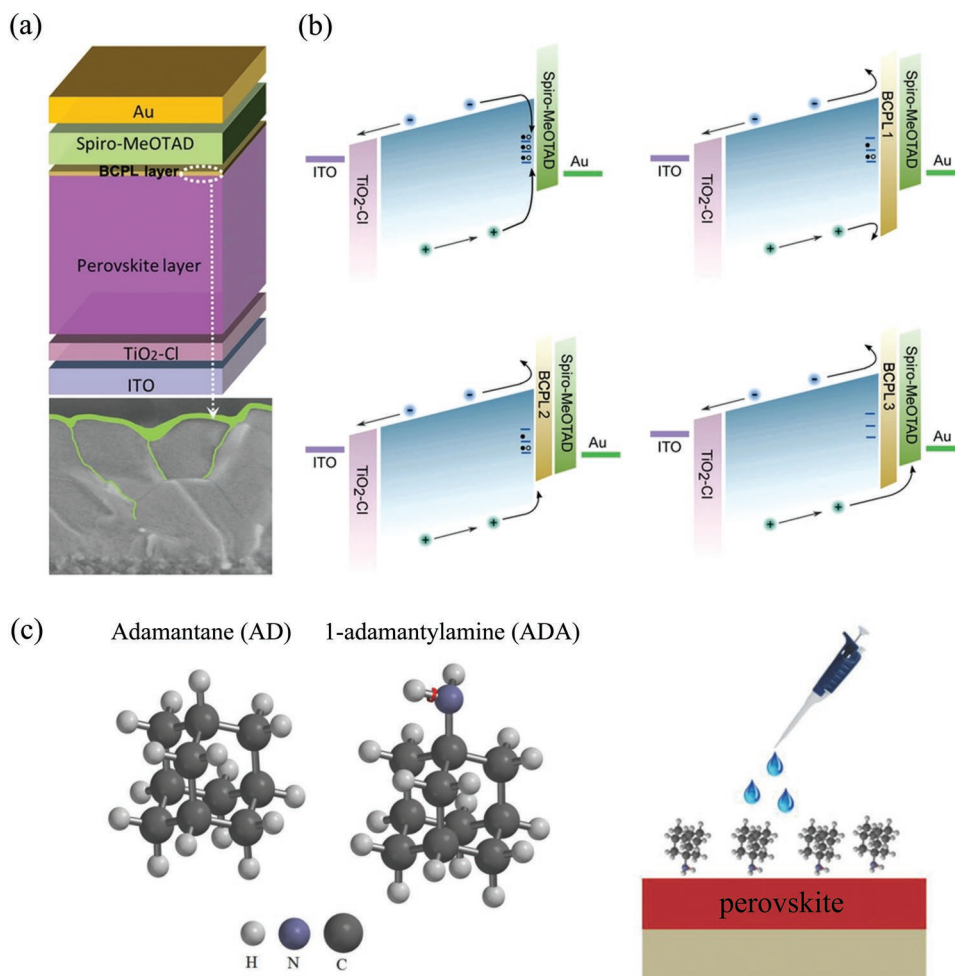


Figure 12. a) Schematic device structure of PSC with a BCPL. b) PSCs without and with BCPL with three possible energy level alignments between the perovskite and BCPL. Reproduced with permission.^[311] Copyright 2019, Wiley-VCH. c) Molecular structure of AD and ADA used for passivation of perovskite film. Reproduced with permission.^[315] Copyright 2018, Wiley-VCH.

6.1.2. Conductive Polymers

At the interface between the perovskite and charge transport layers (ETL or HTL), high defect density appears because of the lattice mismatch, leading to inefficient carrier extraction. Some additives like Li-TFSI (lithium bis(trifluoromethanesulfonyl) imide) could accelerate the disintegration of perovskite even though it is used to improve the hole conduction ability of 2,2',7,7'-tetrakis[N,N-di(4-methoxyphenyl)amino]-9,9'-spirobifluorene (spiro-OMeTAD). Organic semiconductor materials have been developed as the passivation layer and applied to PSC devices, not only adjusting the band alignment but also playing a protective role. As a typical organic semiconductor, the fullerene has been employed to passivate the surface trap states of halide perovskites.^[308] The fullerene layer could intimately contact perovskite and permeate into the perovskite layer along the grain boundaries after a thermal annealing process to reduce the number of surface trapping states.^[308] Both the n-type and p-type semiconducting molecules with Lewis bases as acid functional groups, respectively, have been employed to passivate the grain boundaries of

perovskites.^[309] During the formation of the perovskite film, heterogeneous nucleation of the crystalline solvate (MAPbI₃·DMSO (dimethyl sulfoxide)) is enhanced by the strong interactions between the molecules and precursors, yielding superb passivation layer at perovskite grain boundaries.^[309] The introduction of rubrene with potassium (K₂Rubrene) similarly passivates the perovskite film.^[310] The aromatic rubrene interacts with organic cations of the perovskite, immobilizing them and yielding homogeneous perovskite films. This approach achieves PCE over 19% with suppressed hysteresis.^[310] The interfacial recombination between perovskite and hole transport layer can be suppressed by in situ back-contact passivation (BCP) using a semiconducting polymer, as shown in Figure 12a. Three types of polymers were chosen as the BCP layer candidates: HOMO of -7.2 eV, a shallow HOMO of -5.1 eV, and a middle HOMO of -5.5 eV as shown in Figure 12b. The lower HOMO will block the hole transport. While the higher HOMO in principle provides the largest driving force for charge transfer, but it also leads to increased energy loss, resulting in decrease of V_{OC} . The flat-band alignment between the perovskite and polymer passivation layers leads to better efficiency because of the better charge extraction

ability and energy level structure. As a result, a remarkable PCE of 21.9% with a high V_{OC} of 1.15 V and FF of 83% is obtained.^[311]

6.1.3. Insulative Polymers

Insulative polymers have also been utilized to passivate the perovskite surfaces and enhance device stability because of their hydrophobicity. In fact, the insulative polymers will also block the transmission of carriers. But the high charge mobility of the perovskite causes the carriers penetration across the thin insulative polymer layers. Furthermore, thanks to their hydrophobicity, the stability of PSC devices can be dramatically improved. For example, the carbonyl (C=O) groups of the ultrathin PMMA passivates Pb^{2+} ions of perovskite, effectively reducing nonradiative recombination.^[312] An amazing V_{OC} of 1.22 V with the perovskite bandgap of 1.6 eV is achieved using this Lewis base solution processing step.^[312] When the perovskite films are dipped into the sulfur-oleylamine solution for surface treatment, the ultrathin layer of oleylammonium polysulfides self-assembles on the etched perovskite film, resulting in remarkably increased stability in moisture.^[313] However, the insulating polymers suppress the carriers transport. To optimize performance, the thickness of the polymer interlayer should be controlled precisely. For spin-coating technology, one efficient method is to mix the polymers and antisolvent, resulting in an ultrathin passivation layer after the solvent-extraction process. Grätzel and co-workers introduced PMMA as the passivation layer to the perovskite device by this method.^[314] In their work, PMMA is regarded as a template to control nucleation and crystal growth. The C=O bond from PMMA interacts with the Lewis acid PbI_2 , leading to slower crystal growth and improved perovskite film crystallinity. In addition, adamantane (AD) and 1-adamantylamine (ADA) can also abate electronic defects at the perovskite-hole conductor interface.^[315] The AD and ADA are mixed with the antisolvent or spin coated onto the perovskite surface, as shown in Figure 12c. The XRD patterns of perovskite layers modified by AD and ADA molecules show that the crystal structures remain the same as the reference sample. But the results of TRPL and $I-V$ test demonstrate the less nonradiative carrier recombination and better device performance in this method. The spin coating with the additives is better than the antisolvent method. Furthermore, the contact angle of water on top of the reference sample and the films passivated by AD/ADA were measured, indicating worse wettability for the perovskite films modified with AD and ADA.^[315] Although the insulative polymers suppress the charge mobility at the interfaces of perovskites and charge transport layers, the stability and charge collection efficiency of PSCs are improved by passivating interface defects and isolating the perovskite from moisture. The optimized thickness of the insulative layer not only maintains high conductivity, but also greatly reduces charge recombination caused by defects.

6.2. Inorganic Halide Perovskite Devices

Cesium-based trihalide inorganic perovskites ($CsPbX_3$) have seen rapid improvements because of their thermal stability. Among these perovskites, $CsPbI_3$ is preferred for light harvesting

because of the most suitable bandgap (1.73 eV). However, the small cesium ion in the A site makes it easy to undergo a phase transformation to the orthorhombic phase. Several attempts have been adopted to prevent such a phase transformation so as to retain the narrow band-gap structure (black phase) such as bromine doping. However, Br doping could enlarge the bandgap of the black-phase perovskites. Moreover, phase separation will occur under illumination in mixed halide $CsPb(I_{1-x}Br_x)_3$ materials because of the differential migration of I^- and Br^- .^[316] Another way to stabilize the $CsPbI_3$ black phase is by synthesizing the colloidal QDs, because increasing the surface energy inhibits the phase transition.^[317] The stronger force around the materials can prevent the phase transformation. Since these organic ligands suppress carrier mobility, PCE of $CsPbI_3$ QDs solar cells is unfortunately lower than that of the film devices. Similar to the organic and inorganic hybrid perovskites, there are many defects at the interfaces of inorganic PSCs. In addition to the stabilization of black phase, many works have focused on the interfaces of inorganic perovskite and charge transport layers for improving the performance of the solar cells.

6.2.1. Halide Salts

Like organic-inorganic hybrid perovskite, the halide vacancies are also deep defects in inorganic perovskites. Therefore, halide salts would passivate the defects caused by halide vacancies. For example, phenylethylamine cation (PEA) halide was introduced to passivate the surface of inorganic perovskite and improve the phase stability. The aromatic group of PEA^+ bonds with different halide ions to form a hydrophobic layer on the surface of $CsPbI_2Br$ layer. In addition, Cl^- from PEA was doped into perovskite lattice.^[318] Similarly, PEAI was demonstrated as a passivation layer to decrease the surface defect states.^[319] PEAI acts as a capping layer instead of reaction with $CsPbI_3$ to form the 2D-structured PEA_2PbI_4 .^[319] Recently, the phenyltrimethylammonium bromide (PTABr) was introduced to passivate $CsPbI_3$ perovskite films with a similar approach.^[320] The hydrophobic organic PTA cation caps the $CsPbI_3$ surface and Br ion exchanged I ion from the perovskite lattice, leading to an improved stability. As a result, PCE of the solar cell was up to 17.06%.^[320] In addition, PTABr was introduced into the $CsPbI_3$ QD solution as the ligand exchange, the schematic diagram is shown in Figure 13a.^[321] The PTABr not only passivates the surface defects of QDs, but also improves the carrier mobility of QDs film due to short-chain length of PTABr. A spray-coating technology as a scalable fabrication process was developed to form the large area $CsPbI_3$ QD film (10×10 cm logo) using PTABr- $CsPbI_3$ QDs as shown in Figure 13b. Embedded UV-vis absorption spectra indicate high homogeneity of the film. The QD solar cell fabricated by spray coating shows high PCE of 11.2% with the V_{OC} increased from 1.02 to 1.11 V (Figure 13c) and the stability of the QD devices was also improved (Figure 13d). It can be attributed to the enhancement of hydrophobicity, as shown in Figure 13e.^[321] In addition, choline iodine (CHI) was also introduced to modify the surface of inorganic perovskites. CHI penetrates into the bulk of $CsPbI_3$ thin films, reducing the influence of cracks and pinholes. This CHI treatment improves the energy-level alignment of the CB minimum between $CsPbI_3$ and TiO_2 by 120 meV and increases the lifetime

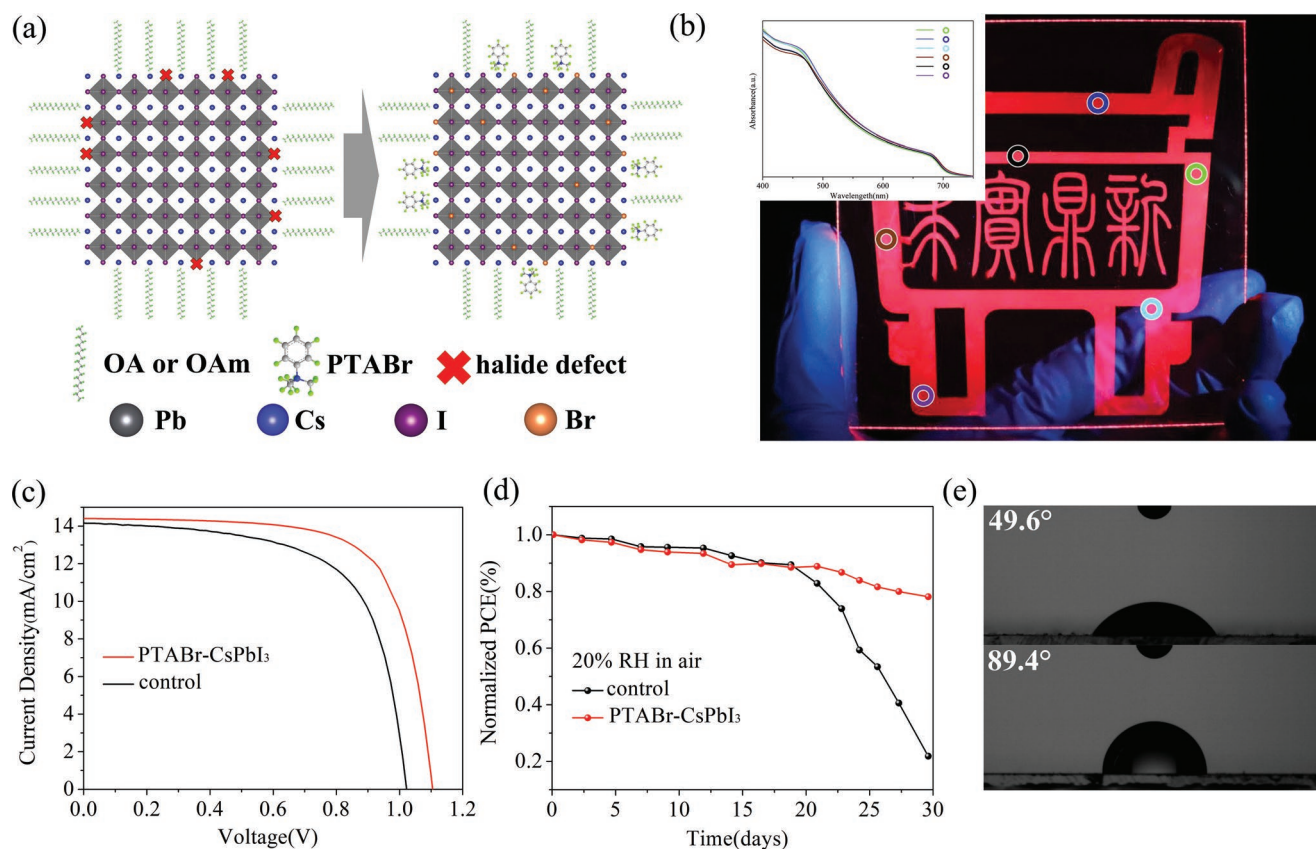


Figure 13. a) Schematic diagram of PTABr ligand passivation. b) Photograph of spray-coated QD films on a $10 \times 10 \text{ cm}^2$ substrate with a complex pattern under UV light excitation. Inset shows UV-vis absorption spectra of the different points on the pattern. c) J - V curves for the passivated QD devices and controls, respectively. d) Statistical PCE distribution for the PSCs of PTABr- CsPbI_3 QDs and controls. h) Long-term stability of PTABr passivated device and controls stored without encapsulation (RH \approx 20%). e) Photographs of the water contact angle for the film sprayed by CsPbI_3 QDs and PTABr- CsPbI_3 QDs. Adapted with permission.^[321] Copyright 2019, Wiley-VCH.

of carriers. Finally, not only the passivation of the surface trap states but also a better matching of the energy levels in CsPbI_3 are achieved. The PCE of the CsPbI_3 film solar cell achieves the record PEC of 18.3% with dependable repeatability and stability.^[322]

6.2.2. Polymers

The inorganic perovskites are particularly sensitive to the humidity and resulting phase transformations. Hydrophobic polymers act a water-proof layer of the inorganic perovskite devices to enhance their stability. Poly(3-hexylthiophene) (P3HT) is one of the typical hole transport materials in organic solar cells. Consequently, P3HT was introduced to the inorganic perovskite device as the HTL. The structure of the device and the cross-sectional SEM image can be seen in **Figure 14a,b**. It also will passivate the surface of inorganic perovskite films to reduce the trap density, as shown in **Figure 14c**.^[323] Meanwhile, P3HT as the hole acceptor will adjust the band energy and increase hole extraction (**Figure 14d**), resulting in the high performance of the solar cells with the best PCE of 12.02%. These have been verified by the TRPL spectra, showing lower trap density.^[323] Finally, the performance of the devices with

spiro-OMeTAD is inferior to P3HT as the HTL resulting in the average V_{OC} increasement about 0.15 V. Moreover, P3HT-based device behaves better stability. Another polymer, poly-vinylpyrrolidone (PVP), was introduced to passivate CsPbI_3 films by surface engineering.^[324] The cubic CsPbI_3 is stabilized by bonding between oxygen atoms of acylamino group and cesium ions in perovskite. As a result, the trap states are immensely reduced and achieved the PCE of 10.74% with high stability.^[324] Similar to PVP, polyethylene glycol not only passivates the surface traps of perovskite but also improves the perovskite film morphology and coverage, achieving increased V_{OC} from 1.11 to 1.28 V.^[325]

6.2.3. Other Passivation

Lead salts can be adopted to passivate Pb^{2+} vacancies which is calculated by DFT as a type of deep trap state and can form on the surface of perovskite. **Figure 15a** demonstrates a Pb^{2+} solution post-processing strategy to passivate deep surface trap states.^[326] Pb vacancies are replaced with Pb^{2+} (**Figure 15b**). The TRPL and space-charge limited current measurements indicate the reduction of defect states, leading to better photoelectric performance with high V_{OC} of 1.29 V and PCE of 12.34%.^[326] Previous work reported aminoethanethiol (AET) as a ligand to

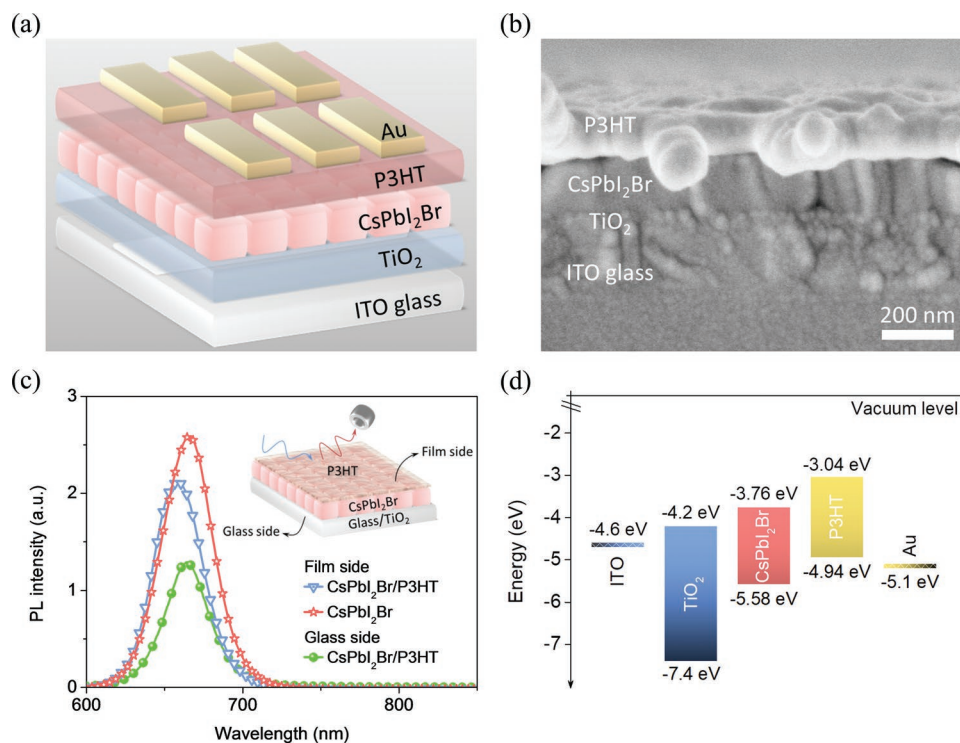


Figure 14. a) Device structure of CsPbI₂Br solar cells. b) Cross-sectional SEM image of a CsPbI₂Br device without Au electrode. c) The steady-state PL spectra for CsPbI₂Br films with P3HT layer using a 405 nm laser as the excitation source from the perovskite film side. d) Schematic energy level diagram. Adapted with permission.^[323] Copyright 2018, Wiley-VCH.

bridge the organic compound (MAI) and inorganic compound (PbI₂) in MAPbI₃ precursor, resulting in uniform perovskite film morphology.^[327] The AET-based perovskite film shows excellent intrinsic water resistance, with the perovskite crystal structure surviving for a long time (>10 min) after immersion in water.^[327] Subsequently, AET was introduced into CsPbI₃ QDs by ligand exchange. The phase stability is enhanced greatly due to the hydrophobicity of AET. The CsPbI₃ QDs films are still luminescent even after immersing in water, which demonstrates an efficient approach for improving the stability of CsPbI₃ QD solar cells.^[328] Nanosheet and QDs of CsPbI₂Br are introduced to passivate CsPbI₂Br bulk film, forming a 3D–2D–0D dimension-profiled interface structure. By changing the energy level of the CsPbI₂Br, a graded band-energy queue can improve the electron extraction and collection at the interface of CsPbI₂Br/perovskite. The efficiency of the device is up to 12.39%. Moreover, the device stability is prominently enhanced because of the higher phase transformation energy of QDs.^[329]

7. Concluding Remarks

Interfaces and interphases determine the redox kinetics, chemical activities, and component compatibility in RBs, and charge transfer and collection in multi-layer structural halide perovskite photovoltaics. Significant research effort has focused on tailoring these interfaces to enhance energy conversion and storage efficiencies, stability, and lifespan of these devices.

RBs: Ion migration and electron transfer occur at the solid–liquid interface in conventional batteries, and at the solid–solid

interface in SSBs. Wettability, chemical stability, and compatibility of components determine battery performance. Surface energy and chemical bond strength are physical–chemical properties that can be subjected to deeper scientific consideration for material modifications. Surface defects such as oxygen vacancies and disordered layers are often desirable to promote electrochemical activity. These defects can be introduced by doping and heat treatment with controlled atmospheres. Artificial layers can prevent cation dissolution from cathodes, and inhibit dendrite growth or surface passivation at anodes. A good artificial layer for electrodes in liquid-electrolyte batteries would possess: 1) chemical inertness but favorable wettability with the liquid electrolyte, 2) high electronic and ionic conductivities, and 3) high mechanical robustness for accommodating the volume change of electrode materials during cycling. In SSBs, the artificial layer should be chemically and mechanically compatible with the electrodes and have high ionic conductivity. The distribution of electrons and ions at the interface has been understudied but should be taken into consideration in the system design. Beyond the study of crystal structure, investigating the electronic structure and chemical bond strength using different spectroscopic techniques (e.g., electron energy loss spectroscopy (EELS) and X-ray absorption fine structure) provides a more holistic understanding of the requirements for battery interfaces and interphases.

Halide PSCs: For the multi-layer structural PSC, the large area of interfaces provides easy pathways for charge recombination, and surface defects and connections between adjacent layers may retard effective charge injection and charge transport, leading to a loss of PCE. Thus, the current and future efforts focus on controlling and passivating the interfaces of carrier

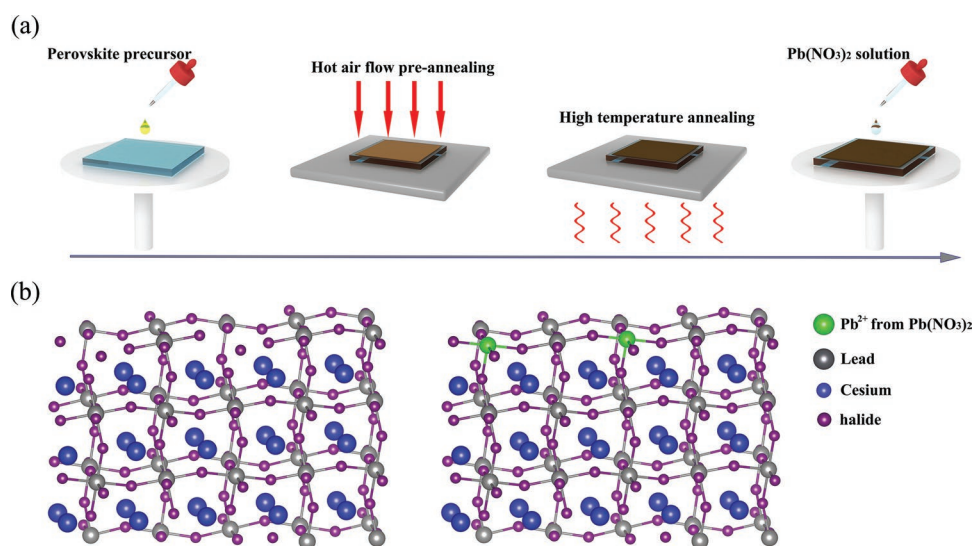


Figure 15. a) Schematic of fabrication process of perovskite films and passivation process using Pb(NO₃)₂ methyl acetate solution. b) Schematic diagram for the defects of the perovskite surface passivated by Pb²⁺ ions. Reproduced with permission.^[326] Copyright 2018, Wiley-VCH.

transport and halide perovskite layers, including: a) adjusting and balancing the band gap structure for more suitable energy level; b) increasing the charge mobility of carrier transport layers for better charge extraction and collection; c) passivating surface defects and traps of perovskites to reduce charge recombination; d) introducing an interlayer to protect perovskite from moisture, oxidation, and photoactive reaction. Commercialization of halide perovskite films will be vitally important, but the scalable fabrication processes, like spray coating,^[330–332] blading,^[333,334] and pressure processing methods^[335,336] cannot obtain high efficiency PSCs as well as the lab-scale devices fabricated by spin-coating method. We speculate that the more defects exist at the interface between each layer due to the nonuniformity of the scalable methods. For HTLs, finding inexpensive p-type materials also contributes to realize commercial manufacturing. Spiro-OMeTAD and PTAA are widely used because of the suitable band energy and good connection with perovskite. But the additive of Li-TFSI in spiro-OMeTAD is hydrophilic, resulting in the acceleration of perovskite degradation. Carbon is a promising candidate of HTL because of the low-cost and matched band level to perovskite. But the conversion efficiency of the carbon-based PSCs is low and the interface between carbon and perovskite still needs to be optimized to enhance the efficiency. Furthermore, many types of polymers have to be inserted as interlayers to protect perovskite from moisture and oxidation. However, the most of these materials are insulating, which hurts charge extraction. To find a hydrophobic semiconductor with appropriate bandgap as the interlayer will be a better way to enhance the device stability without compromising the efficiency.

It is generally true that a defect-free surface is desirable for PSCs, so as to minimize charge trapping and recombination, while highly energetic battery electrode surfaces promote redox reactions. Therefore, RBs benefit from surface defects such as vacancies and impurities, while defects should be minimized and eliminated from PSC surfaces. The strategies to intentionally introduce surface defects in RBs suggest

guidelines to minimize and eliminate surface defects in PSCs during the materials synthesis, processing, and device fabrication steps.

Acknowledgements

C.L., J.Y., and R.M. contributed equally to this work. This work was supported by the National Science Foundation (CBET-1803256), National Key R&D Program of China (2017YFE0119700), National Science Foundation of China (51961135107, 51774034, 51772026), and Beijing Natural Science Foundation (2182039).

Conflict of Interest

The authors declare no conflict of interest.

Keywords

interfaces, interphases, perovskite solar cells, rechargeable batteries, surfaces

Received: August 14, 2019
Revised: October 25, 2019
Published online: January 24, 2020

- [1] D. Larcher, J. M. Tarascon, *Nat. Chem.* **2015**, *7*, 19.
- [2] M. Hosenuzzaman, N. A. Rahim, J. Selvaraj, M. Hasanuzzaman, A. B. M. A. Malek, A. Nahar, *Renewable Sustainable Energy Rev.* **2015**, *41*, 284.
- [3] M. Armand, J. M. Tarascon, *Nature* **2008**, *451*, 652.
- [4] M. Salanne, B. Rotenberg, K. Naoi, K. Kaneko, P. L. Taberna, C. P. Grey, B. Dunn, P. Simon, *Nat. Energy* **2016**, *1*, 16070.
- [5] Y. Rong, Y. Hu, A. Mei, H. Tan, M. I. Saidaminov, S. I. Seok, M. D. McGehee, E. H. Sargent, H. Han, *Science* **2018**, *361*, eaat8235.

- [6] D. Bresser, K. Hosoi, D. Howell, H. Li, H. Zeisel, K. Amine, S. Passerini, *J. Power Sources* **2018**, *382*, 176.
- [7] Z. Li, T. R. Klein, D. H. Kim, M. Yang, J. J. Berry, M. F. A. M. van Hest, K. Zhu, *Nat. Rev. Mater.* **2018**, *3*, 18017.
- [8] J. Ding, W. Hu, E. Paek, D. Mitlin, *Chem. Rev.* **2018**, *118*, 6457.
- [9] A. Kojima, K. Teshima, Y. Shirai, T. Miyasaka, *J. Am. Chem. Soc.* **2009**, *131*, 6050.
- [10] M. Liu, M. B. Johnston, H. J. Snaith, *Nature* **2013**, *501*, 395.
- [11] N. J. Jeon, J. H. Noh, Y. C. Kim, W. S. Yang, S. Ryu, S. I. Seok, *Nat. Mater.* **2014**, *13*, 897.
- [12] H. Tan, A. Jain, O. Voznyy, X. Lan, F. P. Garcia de Arquer, J. Z. Fan, R. Quintero-Bermudez, M. Yuan, B. Zhang, Y. Zhao, F. Fan, P. Li, L. N. Quan, Y. Zhao, Z. H. Lu, Z. Yang, S. Hoogland, E. H. Sargent, *Science* **2017**, *355*, 722.
- [13] W. S. Yang, B. W. Park, E. H. Jung, N. J. Jeon, Y. C. Kim, D. U. Lee, S. S. Shin, J. Seo, E. K. Kim, J. H. Noh, S. I. Seok, *Science* **2017**, *356*, 1376.
- [14] F. Huang, M. Li, P. Siffalovic, G. Cao, J. Tian, *Energy Environ. Sci.* **2019**, *12*, 518.
- [15] E. H. Jung, N. J. Jeon, E. Y. Park, C. S. Moon, T. J. Shin, T. Y. Yang, J. H. Noh, J. Seo, *Nature* **2019**, *567*, 511.
- [16] R. J. Sutton, G. E. Eperon, L. Miranda, E. S. Parrott, B. A. Kamino, J. B. Patel, M. T. Hörantner, M. B. Johnston, A. A. Haghighirad, D. T. Moore, H. J. Snaith, *Adv. Energy Mater.* **2016**, *6*, 1502458.
- [17] D. W. deQuilettes, S. M. Vorpahl, S. D. Stranks, H. Nagaoka, G. E. Eperon, M. E. Ziffer, H. J. Snaith, D. S. Ginger, *Science* **2015**, *348*, 683.
- [18] Q. Han, J. Ding, Y. Bai, T. Li, J.-Y. Ma, Y.-X. Chen, Y. Zhou, J. Liu, Q.-Q. Ge, J. Chen, J. T. Glass, M. J. Therien, J. Liu, D. B. Mitzi, J.-S. Hu, *Chem* **2018**, *4*, 2405.
- [19] D. Shi, V. Adinolfi, R. Comin, M. Yuan, E. Alarousu, A. Buin, Y. Chen, S. Hoogland, A. Rothenberger, K. Katsiev, Y. Losovyj, X. Zhang, P. A. Dowben, O. F. Mohammed, E. H. Sargent, O. M. Bakr, *Science* **2015**, *347*, 519.
- [20] D. P. McMeekin, G. Sadoughi, W. Rehman, G. E. Eperon, M. Saliba, M. T. Horantner, A. Haghighirad, N. Sakai, L. Korte, B. Rech, M. B. Johnston, L. M. Herz, H. J. Snaith, *Science* **2016**, *351*, 151.
- [21] Y. Liu, Z. Yang, D. Cui, X. Ren, J. Sun, X. Liu, J. Zhang, Q. Wei, H. Fan, F. Yu, X. Zhang, C. Zhao, S. F. Liu, *Adv. Mater.* **2015**, *27*, 5176.
- [22] NREL Best Research-Cell Efficiencies, <https://www.nrel.gov/pv/assets/images/efficiency-chart.png> (accessed: April 2019).
- [23] J.-P. Correa-Baena, A. Abate, M. Saliba, W. Tress, T. Jesper Jacobsson, M. Grätzel, A. Hagfeldt, *Energy Environ. Sci.* **2017**, *10*, 710.
- [24] T.-H. Han, S. Tan, J. Xue, L. Meng, J. W. Lee, Y. Yang, *Adv. Mater.* **2019**, *31*, 1803515.
- [25] Y. Liu, D. Liu, Q. Zhang, G. Cao, *J. Mater. Chem.* **2011**, *21*, 9969.
- [26] Z. Wei, D. Wang, X. Yang, C. Wang, G. Chen, F. Du, *Adv. Mater. Interfaces* **2018**, *5*, 1800639.
- [27] D. A. Kitchev, Z. Lun, W. D. Richards, H. Ji, R. J. Clement, M. Balasubramanian, D.-H. Kwon, K. Dai, J. K. Papp, T. Lei, B. D. McCloskey, W. Yang, J. Lee, G. Ceder, *Energy Environ. Sci.* **2018**, *11*, 2159.
- [28] L. Peng, Y. Zhu, D. Chen, R. S. Ruoff, G. Yu, *Adv. Energy Mater.* **2016**, *6*, 1600025.
- [29] Y. S. Tian, T. Shi, W. D. Richards, J. C. Li, J. C. Kim, S. H. Bo, G. Ceder, *Energy Environ. Sci.* **2017**, *10*, 1150.
- [30] J. B. Goodenough, K.-S. Park, *J. Am. Chem. Soc.* **2013**, *135*, 1167.
- [31] A. Jossen, *J. Power Sources* **2006**, *154*, 530.
- [32] D. Aurbach, B. Markovsky, M. D. Levi, E. Levi, A. Schechter, M. Moshkovich, Y. Cohen, *J. Power Sources* **1999**, *81–82*, 95.
- [33] P. B. Balbuena, Y. Wang, *Lithium-Ion Batteries: Solid Electrolyte Interphase*, Imperial College Press, London **2004**.
- [34] J.-K. Park, *Principles and Applications of Lithium Secondary Batteries*, Wiley-VCH, Germany **2012**.
- [35] S. Zhang, K. Zhao, T. Zhu, J. Li, *Prog. Mater. Sci.* **2017**, *89*, 479.
- [36] X. Li, X. Sun, *Adv. Funct. Mater.* **2018**, *28*, 1801323.
- [37] K. Miyano, M. Yanagida, N. Tripathi, Y. Shirai, *J. Phys. Chem. Lett.* **2016**, *7*, 2240.
- [38] J. P. Correa-Baena, A. Abate, M. Saliba, W. Tress, T. J. Jacobsson, M. Grätzel, A. Hagfeldt, *Energy Environ. Sci.* **2017**, *10*, 710.
- [39] W. Nie, H. Tsai, R. Asadpour, J. C. Blancon, A. J. Neukirch, G. Gupta, J. J. Crochet, M. Chhowalla, S. Tretiak, M. A. Alam, H. L. Wang, A. D. Mohite, *Science* **2015**, *347*, 522.
- [40] C. W. Chen, H. W. Kang, S. Y. Hsiao, P. F. Yang, K. M. Chiang, H. W. Lin, *Adv. Mater.* **2014**, *26*, 6647.
- [41] L. Zheng, D. Zhang, Y. Ma, Z. Lu, Z. Chen, S. Wang, L. Xiao, Q. Gong, *Dalton Trans.* **2015**, *44*, 10582.
- [42] J. Kim, A. Ho-Baillie, S. Huang, *Sol. RRL* **2019**, *3*, 1800302.
- [43] T. H. Han, S. Tan, J. Xue, L. Meng, J. W. Lee, Y. Yang, *Adv. Mater.* **2019**, *31*, 1803515.
- [44] W.-J. Yin, T. Shi, Y. Yan, *Appl. Phys. Lett.* **2014**, *104*, 063903.
- [45] H. Uratani, K. Yamashita, *J. Phys. Chem. Lett.* **2017**, *8*, 742.
- [46] A. Buin, P. Pietsch, J. Xu, O. Voznyy, A. H. Ip, R. Comin, E. H. Sargent, *Nano Lett.* **2014**, *14*, 6281.
- [47] H. B. Gray, *Nat. Chem.* **2009**, *1*, 7.
- [48] G. Crabtree, *Nature* **2015**, *526*, S92.
- [49] Z. Yang, J. Zhang, M. C. W. Kintner-Meyer, X. Lu, D. Choi, J. P. Lemmon, J. Liu, *Chem. Rev.* **2011**, *111*, 3577.
- [50] P. Simon, Y. Gogotsi, *Nat. Mater.* **2008**, *7*, 845.
- [51] M. R. Palacin, *Chem. Soc. Rev.* **2009**, *38*, 2565.
- [52] M. Winter, R. J. Brodd, *Chem. Rev.* **2004**, *104*, 4245.
- [53] D. P. Dubal, O. Ayyad, V. Ruiz, P. Gomez-Romero, *Chem. Soc. Rev.* **2015**, *44*, 1777.
- [54] V. Aravindan, J. Gnanaraj, Y.-S. Lee, S. Madhavi, *Chem. Rev.* **2014**, *114*, 11619.
- [55] H. Wang, C. Zhu, D. Chao, Q. Yan, H. J. Fan, *Adv. Mater.* **2017**, *29*, 1702093.
- [56] V. Aravindan, Y. S. Lee, *J. Phys. Chem. Lett.* **2018**, *9*, 3946.
- [57] J. B. Goodenough, Y. Kim, *Chem. Mater.* **2010**, *22*, 587.
- [58] M. S. Whittingham, C. Siu, J. Ding, *Acc. Chem. Res.* **2018**, *51*, 258.
- [59] M. S. Whittingham, *Chem. Rev.* **2014**, *114*, 11414.
- [60] R. C. Massé, C. Liu, Y. Li, L. Mai, G. Cao, *Natl. Sci. Rev.* **2017**, *4*, 26.
- [61] K. Xu, *Chem. Rev.* **2004**, *104*, 4303.
- [62] K. Xu, *Chem. Rev.* **2014**, *114*, 11503.
- [63] C. Liu, G. Cao, in *Nanomaterials for Energy Conversion and Storage* (Eds: D. Wang, G. Cao), World Scientific, Europe **2018**, pp. 397–451.
- [64] J. B. Goodenough, *Energy Storage Mater.* **2015**, *1*, 158.
- [65] J. B. Goodenough, *Acc. Chem. Res.* **2013**, *46*, 1053.
- [66] K. T. Lee, S. Jeong, J. Cho, *Acc. Chem. Res.* **2013**, *46*, 1161.
- [67] J. B. Goodenough, *Chem. Mater.* **2014**, *26*, 820.
- [68] B. C. Melot, J. M. Tarascon, *Acc. Chem. Res.* **2013**, *46*, 1226.
- [69] P. Yan, J. Zheng, J. Zheng, Z. Wang, G. Teng, S. Kuppen, J. Xiao, G. Chen, F. Pan, J.-G. Zhang, C. M. Wang, *Adv. Energy Mater.* **2016**, *6*, 1502455.
- [70] H. Lin, X. Wang, *Adv. Funct. Mater.* **2016**, *26*, 1580.
- [71] Y. Xiao, P. F. Wang, Y. X. Yin, Y. F. Zhu, Y. B. Niu, X. D. Zhang, J. Zhang, X. Yu, X. D. Guo, B.-H. Zhong, Y. G. Guo, *Adv. Mater.* **2018**, *30*, 1803765.
- [72] G. Liu, H. G. Yang, J. Pan, Y. Q. Yang, G. Q. Lu, H.-M. Cheng, *Chem. Rev.* **2014**, *114*, 9559.
- [73] W. Sun, F. Cao, Y. Liu, X. Zhao, X. Liu, J. Yuan, *J. Mater. Chem.* **2012**, *22*, 20952.
- [74] S. Joshi, S. Lanka, S. J. Ippolito, S. K. Bhargava, M. V. Sunkara, *J. Mater. Chem. A* **2016**, *4*, 16418.
- [75] J. Kalhoff, G. Eshetu Gebrekidan, D. Bresser, S. Passerini, *ChemSusChem* **2015**, *8*, 2154.

- [76] A. M. Haregewoin, A. S. Wotango, B. J. Hwang, *Energy Environ. Sci.* **2016**, 9, 1955.
- [77] M. Marcinek, J. Syzdek, M. Marczewski, M. Piszcz, L. Niedzicki, M. Kalita, A. Plewa-Marczewska, A. Bitner, P. Wieczorek, T. Trzeciak, M. Kasprzyk, P. Łęzak, Z. Zukowska, A. Zalewska, W. Wieczorek, *Solid State Ionics* **2015**, 276, 107.
- [78] C. Liu, S. Wang, C. Zhang, H. Fu, X. Nan, Y. Yang, G. Cao, *Energy Storage Mater.* **2016**, 5, 93.
- [79] C. Liu, G. Z. Neale, J. Zheng, X. Jia, J. Huang, M. Yan, M. Tian, M. Wang, J. Yang, G. Cao, *Energy Environ. Sci.* **2019**, 12, 2273.
- [80] J. Huang, X. Guo, X. Du, X. Lin, J.-Q. Huang, H. Tan, Y. Zhu, B. Zhang, *Energy Environ. Sci.* **2019**, 12, 1550.
- [81] B. Wu, S. Wang, J. Lochala, D. Desrochers, B. Liu, W. Zhang, J. Yang, J. Xiao, *Energy Environ. Sci.* **2018**, 11, 1803.
- [82] A. L. Michan, G. Divitini, A. J. Pell, M. Leskes, C. Ducati, C. P. Grey, *J. Am. Chem. Soc.* **2016**, 138, 7918.
- [83] E. Peled, *J. Electrochem. Soc.* **1979**, 126, 2047.
- [84] X. B. Cheng, R. Zhang, C. Z. Zhao, F. Wei, J. G. Zhang, Q. Zhang, *Adv. Sci.* **2016**, 3, 1500213.
- [85] W. Ma, C. Zhang, C. Liu, X. Nan, H. Fu, G. Cao, *ACS Appl. Mater. Interfaces* **2016**, 8, 19542.
- [86] K. Wang, C. Zhang, H. Fu, C. Liu, Z. Li, W. Ma, X. Lu, G. Cao, *Chem. - Eur. J.* **2017**, 23, 5368.
- [87] C. Zhang, K. Wang, C. Liu, X. Nan, H. Fu, W. Ma, Z. Li, G. Cao, *NPG Asia Mater.* **2016**, 8, e287.
- [88] J. B. Goodenough, Y. Kim, *J. Power Sources* **2011**, 196, 6688.
- [89] J. N. Zhang, Q. Li, Y. Wang, J. Zheng, X. Yu, H. Li, *Energy Storage Mater.* **2018**, 14, 1.
- [90] N. S. Choi, J. G. Han, S. Y. Ha, I. Park, C. K. Back, *RSC Adv.* **2015**, 5, 2732.
- [91] J. B. Goodenough, *Energy Environ. Sci.* **2014**, 7, 14.
- [92] X. B. Cheng, C. Yan, X. Q. Zhang, H. Liu, Q. Zhang, *ACS Energy Lett.* **2018**, 3, 1564.
- [93] C. Kittel, *Introduction to Solid State Physics*, 8th ed., Wiley, New York **2005**.
- [94] Y. Kobayashi, H. Miyashiro, T. Takeuchi, H. Shigemura, N. Balakrishnan, M. Tabuchi, H. Kageyama, T. Iwahori, *Solid State Ionics* **2002**, 152–153, 137.
- [95] R. C. Xu, X. H. Xia, Z. J. Yao, X. L. Wang, C. D. Gu, J. P. Tu, *Electrochim. Acta* **2016**, 219, 235.
- [96] M. Kotobuki, K. Kanamura, Y. Sato, T. Yoshida, *J. Power Sources* **2011**, 196, 7750.
- [97] G. Bucci, T. Swamy, Y. M. Chiang, W. C. Carter, *J. Mater. Chem. A* **2017**, 5, 19422.
- [98] M. Nagao, A. Hayashi, M. Tatsumisago, T. Kanetsuku, T. Tsuda, S. Kuwabata, *Phys. Chem. Chem. Phys.* **2013**, 15, 18600.
- [99] T. Liu, Y. Zhang, R. Chen, S. X. Zhao, Y. Lin, C. W. Nan, Y. Shen, *Electrochem. Commun.* **2017**, 79, 1.
- [100] T. Famprikis, P. Canepa, J. A. Dawson, M. S. Islam, C. Masquelier, *Nat. Mater.* **2019**, 18, 1278.
- [101] S. Krueger, R. Kloepsch, J. Li, S. Nowak, S. Passerini, M. Winter, *J. Electrochem. Soc.* **2013**, 160, A542.
- [102] T. Liu, Y. Ren, Y. Shen, S. X. Zhao, Y. Lin, C. W. Nan, *J. Power Sources* **2016**, 324, 349.
- [103] K. Yamamoto, R. Yoshida, T. Sato, H. Matsumoto, H. Kurobe, T. Hamanaka, T. Kato, Y. Iriyama, T. Hirayama, *J. Power Sources* **2014**, 266, 414.
- [104] D. Bar-Tow, E. Peled, L. Burstein, *J. Electrochem. Soc.* **1999**, 146, 824.
- [105] D. Aurbach, Y. Ein-Ely, A. Zaban, *J. Electrochem. Soc.* **1994**, 141, L1.
- [106] J. Christensen, J. Newman, *J. Electrochem. Soc.* **2004**, 151, A1977.
- [107] X. B. Cheng, R. Zhang, C. Z. Zhao, Q. Zhang, *Chem. Rev.* **2017**, 117, 10403.
- [108] A. Yoshino, *Angew. Chem., Int. Ed.* **2012**, 51, 5798.
- [109] M. Li, J. Lu, Z. Chen, K. Amine, *Adv. Mater.* **2018**, 30, 1800561.
- [110] E. Peled, *J. Power Sources* **1983**, 9, 253.
- [111] A. M. Andersson, A. Henningsson, H. Siegbahn, U. Jansson, K. Edström, *J. Power Sources* **2003**, 119–121, 522.
- [112] S.-K. Jeong, M. Inaba, T. Abe, Z. Ogumi, *J. Electrochem. Soc.* **2001**, 148, A989.
- [113] E. Peled, D. Golodnitsky, G. Ardel, *J. Electrochem. Soc.* **1997**, 144, L208.
- [114] X. Yu, A. Manthiram, *Acc. Chem. Res.* **2017**, 50, 2653.
- [115] D. Aurbach, I. Weissman, A. Zaban, O. Chusid, *Electrochim. Acta* **1994**, 39, 51.
- [116] A. Zaban, E. Zinigrad, D. Aurbach, *J. Phys. Chem.* **1996**, 100, 3089.
- [117] D. Aurbach, A. Zaban, Y. Gofer, Y. E. Ely, I. Weissman, O. Chusid, O. Abramson, *J. Power Sources* **1995**, 54, 76.
- [118] O. Chusid, E. Ein Ely, D. Aurbach, M. Babai, Y. Carmeli, *J. Power Sources* **1993**, 43, 47.
- [119] G. V. Zhuang, K. Xu, H. Yang, T. R. Jow, P. N. Ross, *J. Phys. Chem. B* **2005**, 109, 17567.
- [120] E. Peled, D. Golodnitsky, C. MenaChem, D. Bar-Tow, *J. Electrochem. Soc.* **1998**, 145, 3482.
- [121] D. Bedrov, G. D. Smith, A. C. T. van Duin, *J. Phys. Chem. A* **2012**, 116, 2978.
- [122] S. Laruelle, S. Grugeon, P. Poizot, M. Dollé, L. Dupont, J.-M. Tarascon, *J. Electrochem. Soc.* **2002**, 149, A627.
- [123] P. Balaya, H. Li, L. Kienle, J. Maier, *Adv. Funct. Mater.* **2003**, 13, 621.
- [124] C. Liu, H. Fu, Y. Pei, J. Wu, V. Pisharodi, Y. Hu, G. Gao, R. J. Yang, J. Yang, G. Cao, *J. Mater. Chem. A* **2019**, 7, 7831.
- [125] L. Wang, A. Menakath, F. Han, Y. Wang, P. Y. Zavalij, K. J. Gaskell, O. Borodin, D. Iuga, S. P. Brown, C. Wang, K. Xu, B. W. Eichhorn, *Nat. Chem.* **2019**, 11, 789.
- [126] M. R. Wagner, J. H. Albering, K. C. Moeller, J. O. Besenhard, M. Winter, *Electrochem. Commun.* **2005**, 7, 947.
- [127] K. Xu, Y. Lam, S. S. Zhang, T. R. Jow, T. B. Curtis, *J. Phys. Chem. C* **2007**, 111, 7411.
- [128] K. R. Kneten, R. L. McCreery, *Anal. Chem.* **1992**, 64, 2518.
- [129] R. L. McCreery, *Chem. Rev.* **2008**, 108, 2646.
- [130] Y. Domi, M. Ochida, S. Tsubouchi, H. Nakagawa, T. Yamanaka, T. Doi, T. Abe, Z. Ogumi, *J. Phys. Chem. C* **2011**, 115, 25484.
- [131] M. Gauthier, T. J. Carney, A. Grimaud, L. Giordano, N. Pour, H.-H. Chang, D. P. Fenning, S. F. Lux, O. Paschos, C. Bauer, F. Maglia, S. Lupart, P. Lamp, Y. Shao-Horn, *J. Phys. Chem. Lett.* **2015**, 6, 4653.
- [132] N. Yabuuchi, K. Yoshii, S.-T. Myung, I. Nakai, S. Komaba, *J. Am. Chem. Soc.* **2011**, 133, 4404.
- [133] D. Aurbach, M. D. Levi, E. Levi, H. Teller, B. Markovsky, G. Salitra, U. Heider, L. Heider, *J. Electrochem. Soc.* **1998**, 145, 3024.
- [134] A. L. Michan, B. S. Parimalam, M. Leskes, R. N. Kerber, T. Yoon, C. P. Grey, B. L. Lucht, *Chem. Mater.* **2016**, 28, 8149.
- [135] S. S. Zhang, *J. Power Sources* **2006**, 162, 1379.
- [136] Y. C. Lu, A. N. Mansour, N. Yabuuchi, Y. Shao-Horn, *Chem. Mater.* **2009**, 21, 4408.
- [137] A. Hammami, N. Raymond, M. Armand, *Nature* **2003**, 424, 635.
- [138] P. Ribière, S. Grugeon, M. Morcrette, S. Boyanov, S. Laruelle, G. Marlair, *Energy Environ. Sci.* **2012**, 5, 5271.
- [139] T. Krauskopf, R. Dippel, H. Hartmann, K. Peppler, B. Mogwitz, F. H. Richter, W. G. Zeier, J. Janek, *Joule* **2019**, 3, 2030.
- [140] F. M. Pesci, R. H. Brugge, A. K. O. Hekselman, A. Cavallaro, R. J. Chater, A. Aguadero, *J. Mater. Chem. A* **2018**, 6, 19817.
- [141] W. D. Richards, L. J. Miara, Y. Wang, J. C. Kim, G. Ceder, *Chem. Mater.* **2016**, 28, 266.
- [142] N. D. Lepley, N. A. W. Holzwarth, *Phys. Rev. B* **2015**, 92, 214201.
- [143] L. Porz, T. Swamy, B. W. Sheldon, D. Rettenwander, T. Frömling, H. L. Thaman, S. Berendts, R. Uecker, W. C. Carter, Y. M. Chiang, *Adv. Energy Mater.* **2017**, 7, 1701003.

- [144] X. Yao, N. Huang, F. Han, Q. Zhang, H. Wan, J. P. Mwiizerwa, C. Wang, X. Xu, *Adv. Energy Mater.* **2017**, *7*, 1602923.
- [145] E. Fabbri, D. Pergolesi, E. Traversa, *Sci. Technol. Adv. Mater.* **2010**, *11*, 054503.
- [146] J. Garcia-Barriocanal, A. Rivera-Calzada, M. Varela, Z. Sefrioui, E. Iborra, C. Leon, S. J. Pennycook, J. Santamaria, *Science* **2008**, *321*, 676.
- [147] S. Kim, M. Hirayama, S. Taminato, R. Kanno, *Dalton Trans.* **2013**, *42*, 13112.
- [148] Z. Wang, D. Santhanagopalan, W. Zhang, F. Wang, H. L. Xin, K. He, J. Li, N. Dudney, Y. S. Meng, *Nano Lett.* **2016**, *16*, 3760.
- [149] T. Okumura, T. Nakatsutsumi, T. Ina, Y. Orikasa, H. Arai, T. Fukutsuka, Y. Iriyama, T. Uruga, H. Tanida, Y. Uchimoto, Z. Ogumi, *J. Mater. Chem.* **2011**, *21*, 10051.
- [150] V. Thangadurai, S. Narayanan, D. Pinzar, *Chem. Soc. Rev.* **2014**, *43*, 4714.
- [151] K. Fu, Y. Gong, B. Liu, Y. Zhu, S. Xu, Y. Yao, W. Luo, C. Wang, S. D. Lacey, J. Dai, Y. Chen, Y. Mo, E. Wachsman, L. Hu, *Sci. Adv.* **2017**, *3*, e1601659.
- [152] H. Duan, Y. X. Yin, Y. Shi, P.-F. Wang, X.-D. Zhang, C. P. Yang, J. L. Shi, R. Wen, Y. G. Guo, L. J. Wan, *J. Am. Chem. Soc.* **2018**, *140*, 82.
- [153] F. Hao, X. Chi, Y. Liang, Y. Zhang, R. Xu, H. Guo, T. Terlier, H. Dong, K. Zhao, J. Lou, Y. Yao, *Joule* **2019**, *3*, 1349.
- [154] F. Han, T. Gao, Y. Zhu, K. J. Gaskell, C. Wang, *Adv. Mater.* **2015**, *27*, 3473.
- [155] F. Han, Y. Zhu, X. He, Y. Mo, C. Wang, *Adv. Energy Mater.* **2016**, *6*, 1501590.
- [156] N. Kamaya, K. Homma, Y. Yamakawa, M. Hirayama, R. Kanno, M. Yonemura, T. Kamiyama, Y. Kato, S. Hama, K. Kawamoto, A. Mitsui, *Nat. Mater.* **2011**, *10*, 682.
- [157] S. Ohta, T. Kobayashi, T. Asaoka, *J. Power Sources* **2011**, *196*, 3342.
- [158] C. L. Tsai, V. Roddatis, C. V. Chandran, Q. Ma, S. Uhlenbruck, M. Bram, P. Heitjans, O. Guillon, *ACS Appl. Mater. Interfaces* **2016**, *8*, 10617.
- [159] M. H. Braga, A. J. Murchison, J. A. Ferreira, P. Singh, J. B. Goodenough, *Energy Environ. Sci.* **2016**, *9*, 948.
- [160] M. H. Braga, J. A. Ferreira, A. J. Murchison, J. B. Goodenough, *J. Electrochem. Soc.* **2017**, *164*, A207.
- [161] M. H. Braga, C. M. Subramaniam, A. J. Murchison, J. B. Goodenough, *J. Am. Chem. Soc.* **2018**, *140*, 6343.
- [162] Y. Yoon, C. Park, J. Kim, D. Shin, *J. Power Sources* **2013**, *226*, 186.
- [163] J. Kasemchainan, S. Zekoll, D. Spencer Jolly, Z. Ning, G. O. Hartley, J. Marrow, P. G. Bruce, *Nat. Mater.* **2019**, *18*, 1105.
- [164] F. Jiao, P. G. Bruce, *Adv. Mater.* **2007**, *19*, 657.
- [165] J. Y. Luo, J. J. Zhang, Y. Y. Xia, *Chem. Mater.* **2006**, *18*, 5618.
- [166] B. Kang, G. Ceder, *Nature* **2009**, *458*, 190.
- [167] Y. Z. Zheng, H. Ding, E. Uchaker, X. Tao, J. F. Chen, Q. Zhang, G. Cao, *J. Mater. Chem. A* **2015**, *3*, 1979.
- [168] E. Uchaker, G. Cao, *Chem. - Asian J.* **2015**, *10*, 1608.
- [169] F. Zheng, C. Yang, X. Xiong, J. Xiong, R. Hu, Y. Chen, M. Liu, *Angew. Chem., Int. Ed.* **2015**, *54*, 13058.
- [170] X. Peng, X. Zhang, L. Wang, L. Hu, S. H. S. Cheng, C. Huang, B. Gao, F. Ma, K. Huo, P. K. Chu, *Adv. Funct. Mater.* **2016**, *26*, 784.
- [171] T. Xia, W. Zhang, W. Li, N. A. Oylar, G. Liu, X. Chen, *Nano Energy* **2013**, *2*, 826.
- [172] J. Zheng, L. Liu, G. Ji, Q. Yang, L. Zheng, J. Zhang, *ACS Appl. Mater. Interfaces* **2016**, *8*, 20074.
- [173] J. Y. Shin, J. H. Joo, D. Samuelis, J. Maier, *Chem. Mater.* **2012**, *24*, 543.
- [174] Z. Lu, C. T. Yip, L. Wang, H. Huang, L. Zhou, *ChemPlusChem* **2012**, *77*, 991.
- [175] M. He, Z. Wang, X. Yan, L. Tian, G. Liu, X. Chen, *J. Power Sources* **2016**, *306*, 309.
- [176] L. Shen, E. Uchaker, X. Zhang, G. Cao, *Adv. Mater.* **2012**, *24*, 6502.
- [177] D. Liu, Y. Zhang, P. Xiao, B. B. Garcia, Q. Zhang, X. Zhou, Y. H. Jeong, G. Cao, *Electrochim. Acta* **2009**, *54*, 6816.
- [178] J. Ni, S. Fu, C. Wu, J. Maier, Y. Yu, L. Li, *Adv. Mater.* **2016**, *28*, 2259.
- [179] J. Ni, M. Sun, L. Li, *Adv. Mater.* **2019**, *31*, 1902603.
- [180] J. Yao, Y. Li, R. C. Massé, E. Uchaker, G. Cao, *Energy Storage Mater.* **2018**, *11*, 205.
- [181] S. Mohammadi-Jam, K. E. Waters, *Adv. Colloid Interface Sci.* **2014**, *212*, 21.
- [182] J. A. F. Gamelas, *Cellulose* **2013**, *20*, 2675.
- [183] J. Schultz, L. Lavielle, C. Martin, C. Martin, *J. Adhes.* **1987**, *23*, 45.
- [184] D. Liu, Y. Liu, B. B. Garcia, Q. Zhang, A. Pan, Y. H. Jeong, G. Cao, *J. Mater. Chem.* **2009**, *19*, 8789.
- [185] W. Bi, J. Wang, E. P. Jahrman, G. T. Seidler, G. Gao, G. Wu, G. Cao, *Small* **2019**, *15*, 1901747.
- [186] W. Bi, Y. Wu, C. Liu, J. Wang, Y. Du, G. Gao, G. Wu, G. Cao, *ACS Appl. Energy Mater.* **2019**, *2*, 668.
- [187] W. Bi, E. P. Jahrman, G. T. Seidler, J. Wang, G. Gao, G. Wu, M. Atif, M. S. AlSalhi, G. Cao, *ACS Appl. Mater. Interfaces* **2019**, *11*, 16647.
- [188] W. Bi, J. Huang, M. Wang, E. P. Jahrman, G. T. Seidler, J. Wang, Y. Wu, G. Gao, G. Wu, G. Cao, *J. Mater. Chem. A* **2019**, *7*, 17966.
- [189] T. Aoshima, K. Okahara, C. Kiyohara, K. Shizuka, *J. Power Sources* **2001**, *97–98*, 377.
- [190] D. H. Jang, Y. J. Shin, S. M. Oh, *J. Electrochem. Soc.* **1996**, *143*, 2204.
- [191] H. D. Yoo, I. Shterenberg, Y. Gofer, G. Gershinshy, N. Pour, D. Aurbach, *Energy Environ. Sci.* **2013**, *6*, 2265.
- [192] C. Zhan, T. Wu, J. Lu, K. Amine, *Energy Environ. Sci.* **2018**, *11*, 243.
- [193] K. Park, J. Kim, J. H. Park, Y. Hwang, D. Han, *J. Power Sources* **2018**, *408*, 105.
- [194] Y. Zhao, J. Liu, S. Wang, R. Ji, Q. Xia, Z. Ding, W. Wei, Y. Liu, P. Wang, D. G. Ivey, *Adv. Funct. Mater.* **2016**, *26*, 4760.
- [195] A. Jana, R. E. Garcia, *Nano Energy* **2017**, *41*, 552.
- [196] T. Gupta, A. Kim, S. Phadke, S. Biswas, T. Luong, B. J. Hertzberg, M. Chamoun, K. Evans-Lutterodt, D. A. Steingart, *J. Power Sources* **2016**, *305*, 22.
- [197] B. Sun, P. Li, J. Zhang, D. Wang, P. Munroe, C. Wang, P. H. L. Notten, G. Wang, *Adv. Mater.* **2018**, *30*, 1801334.
- [198] X. Wang, W. Zeng, L. Hong, W. Xu, H. Yang, F. Wang, H. Duan, M. Tang, H. Jiang, *Nat. Energy* **2018**, *3*, 227.
- [199] S. B. Son, T. Gao, S. P. Harvey, K. X. Steirer, A. Stokes, A. Norman, C. Wang, A. Cresce, K. Xu, C. Ban, *Nat. Chem.* **2018**, *10*, 532.
- [200] R. Attias, M. Salama, B. Hirsch, Y. Goffer, D. Aurbach, *Joule* **2019**, *3*, 27.
- [201] J. Xie, J. Wang, H. R. Lee, K. Yan, Y. Li, F. Shi, W. Huang, A. Pei, G. Chen, R. Subbaraman, J. Christensen, Y. Cui, *Sci. Adv.* **2018**, *4*, eaat5168.
- [202] J. Zhu, P. Li, X. Chen, D. Legut, Y. Fan, R. Zhang, Y. Lu, X. Cheng, Q. Zhang, *Energy Storage Mater.* **2019**, *16*, 426.
- [203] J. Lopez, A. Pei, J. Y. Oh, G. J. N. Wang, Y. Cui, Z. Bao, *J. Am. Chem. Soc.* **2018**, *140*, 11735.
- [204] B. Zhu, Y. Jin, X. Hu, Q. Zheng, S. Zhang, Q. Wang, J. Zhu, *Adv. Mater.* **2017**, *29*, 1603755.
- [205] N. W. Li, Y. X. Yin, C. P. Yang, Y. G. Guo, *Adv. Mater.* **2016**, *28*, 1853.
- [206] M. Kornbluth, J. Mailoa, B. Kozinsky, G. Samsonidze, J. F. Christensen, *US patent, US20190036120A1*, **2019**.
- [207] J. Zhao, L. Liao, F. Shi, T. Lei, G. Chen, A. Pei, J. Sun, K. Yan, G. Zhou, J. Xie, C. Liu, Y. Li, Z. Liang, Z. Bao, Y. Cui, *J. Am. Chem. Soc.* **2017**, *139*, 11550.
- [208] W. Luo, C. F. Lin, O. Zhao, M. Noked, Y. Zhang, G. W. Rubloff, L. Hu, *Adv. Energy Mater.* **2017**, *7*, 1601526.
- [209] Q. Zhao, Z. Tu, S. Wei, K. Zhang, S. Choudhury, X. Liu, L. A. Archer, *Angew. Chem.* **2018**, *130*, 1004.
- [210] N. W. Li, Y. X. Yin, J. Y. Li, C. H. Zhang, Y. G. Guo, *Adv. Sci.* **2017**, *4*, 1600400.

- [211] J. Zheng, M. H. Engelhard, D. Mei, S. Jiao, B. J. Polzin, J. G. Zhang, W. Xu, *Nat. Energy* **2017**, *2*, 17012.
- [212] E. Markevich, G. Salitra, D. Aurbach, *ACS Energy Lett.* **2017**, *2*, 1337.
- [213] Y. Liu, D. Lin, P. Y. Yuen, K. Liu, J. Xie, R. H. Dauskardt, Y. Cui, *Adv. Mater.* **2017**, *29*, 1605531.
- [214] C. Yan, H.-R. Li, X. Chen, X.-Q. Zhang, X.-B. Cheng, R. Xu, J.-Q. Huang, Q. Zhang, *J. Am. Chem. Soc.* **2019**, *141*, 9422.
- [215] T. Lapp, S. Skaarup, A. Hooper, *Solid State Ionics* **1983**, *11*, 97.
- [216] C. Yan, X. B. Cheng, Y. X. Yao, X. Shen, B. Q. Li, W. J. Li, R. Zhang, J. Q. Huang, H. Li, Q. Zhang, *Adv. Mater.* **2018**, *30*, 1804461.
- [217] G. Zheng, S. W. Lee, Z. Liang, H.-W. Lee, K. Yan, H. Yao, H. Wang, W. Li, S. Chu, Y. Cui, *Nat. Nanotechnol.* **2014**, *9*, 618.
- [218] B. Li, R. Masse, C. Liu, Y. Hu, W. Li, G. Zhang, G. Cao, *Energy Storage Mater.* **2019**, *22*, 96.
- [219] C. Wang, Y. S. Meng, K. Xu, *J. Electrochem. Soc.* **2019**, *166*, A5184.
- [220] Y. Dai, L. Cai, R. E. White, *J. Electrochem. Soc.* **2013**, *160*, A182.
- [221] I. H. Cho, S. S. Kim, S. C. Shin, N. S. Choi, *Electrochem. Solid-State Lett.* **2010**, *13*, A168.
- [222] Z. Chen, Z. Lu, J. R. Dahn, *J. Electrochem. Soc.* **2002**, *149*, A1604.
- [223] J. Kim, H. Lee, H. Cha, M. Yoon, M. Park, J. Cho, *Adv. Energy Mater.* **2018**, *8*, 1702028.
- [224] P. K. Nayak, E. M. Erickson, F. Schipper, T. R. Penki, N. Munichandraiah, P. Adelhelm, H. Sclar, F. Amalraj, B. Markovsky, D. Aurbach, *Adv. Energy Mater.* **2018**, *8*, 1702397.
- [225] J. Zheng, S. Myeong, W. Cho, P. Yan, J. Xiao, C. Wang, J. Cho, J. G. Zhang, *Adv. Energy Mater.* **2017**, *7*, 1601284.
- [226] S. Hwang, W. Chang, S. M. Kim, D. Su, D. H. Kim, J. Y. Lee, K. Y. Chung, E. A. Stach, *Chem. Mater.* **2014**, *26*, 1084.
- [227] W. S. Yoon, K. B. Kim, M. G. Kim, M. K. Lee, H. J. Shin, J. M. Lee, J. S. Lee, C. H. Yo, *J. Phys. Chem. B* **2002**, *106*, 2526.
- [228] Y. Zhou, Y. Lee, H. Sun, J. M. Wallas, S. M. George, M. Xie, *ACS Appl. Mater. Interfaces* **2017**, *9*, 9614.
- [229] H. H. Sun, J. Y. Hwang, C. S. Yoon, A. Heller, C. B. Mullins, *ACS Nano* **2012**, *12*, 12912.
- [230] L. David, K. Dahlberg, D. Mohanty, R. E. Ruther, A. Huq, M. Chi, S. J. An, C. Mao, D. M. King, L. Stevenson, D. L. Wood, *ACS Appl. Energy Mater.* **2019**, *2*, 1308.
- [231] P. Yan, J. Zheng, X. Zhang, R. Xu, K. Amine, J. Xiao, J. G. Zhang, C. M. Wang, *Chem. Mater.* **2016**, *28*, 857.
- [232] S. Hu, Y. Li, Y. Chen, J. Peng, T. Zhou, W. K. Pang, C. Didier, V. K. Peterson, H. Wang, Q. Li, Z. Guo, *Adv. Energy Mater.* **2019**, *9*, 1901795.
- [233] X. D. Zhang, J. L. Shi, J. Y. Liang, Y. X. Yin, J. N. Zhang, X. Q. Yu, Y. G. Guo, *Adv. Mater.* **2018**, *30*, 1801751.
- [234] P. Yan, J. Zheng, J. Liu, B. Wang, X. Cheng, Y. Zhang, X. Sun, C. Wang, J. G. Zhang, *Nat. Energy* **2018**, *3*, 600.
- [235] G. L. Xu, Q. Liu, K. K. S. Lau, Y. Liu, X. Liu, H. Gao, X. Zhou, M. Zhuang, Y. Ren, J. Li, M. Shao, M. Ouyang, F. Pan, Z. Chen, K. Amine, G. Chen, *Nat. Energy* **2019**, *4*, 484.
- [236] Y. K. Sun, Z. Chen, H. J. Noh, D. J. Lee, H. G. Jung, Y. Ren, S. Wang, C. S. Yoon, S. T. Myung, K. Amine, *Nat. Mater.* **2012**, *11*, 942.
- [237] R. P. Qing, J. L. Shi, D. D. Xiao, X. D. Zhang, Y. X. Yin, Y. B. Zhai, L. Gu, Y. G. Guo, *Adv. Energy Mater.* **2016**, *6*, 1501914.
- [238] J. Y. Piao, L. Gu, Z. Wei, J. Ma, J. Wu, W. Yang, Y. Gong, Y. G. Sun, S. Y. Duan, X. S. Tao, D. S. Bin, A. Cao, L. J. Wan, *J. Am. Chem. Soc.* **2019**, *141*, 4900.
- [239] M. Fingerle, R. Buchheit, S. Siculo, K. Albe, R. Hausbrand, *Chem. Mater.* **2017**, *29*, 7675.
- [240] J. Maier, *Physical Chemistry of Ionic Materials: Ions and Electrons in Solids*, Wiley, New York **2004**.
- [241] W. Weppner, in *Materials for Lithium-Ion Batteries* (Eds: C. Julien, Z. Stoyanov), Springer, Netherlands, Dordrecht **2000**, pp. 401–412.
- [242] L. Le Van-Jodin, F. Ducroquet, F. Sabary, I. Chevalier, *Solid State Ionics* **2013**, *253*, 151.
- [243] N. J. J. de Klerk, M. Wagemaker, *ACS Appl. Energy Mater.* **2018**, *1*, 3230.
- [244] N. Ohta, K. Takada, I. Sakaguchi, L. Zhang, R. Ma, K. Fukuda, M. Osada, T. Sasaki, *Electrochem. Commun.* **2007**, *9*, 1486.
- [245] J. Haruyama, K. Sodeyama, L. Han, K. Takada, Y. Tateyama, *Chem. Mater.* **2014**, *26*, 4248.
- [246] N. G. Park, M. Grätzel, T. Miyasaka, *Organic-Inorganic Halide Perovskite Photovoltaics: From Fundamentals to Device Architectures*, Springer, Cham **2016**.
- [247] Q. Chen, N. De Marco, Y. Yang, T.-B. Song, C. C. Chen, H. Zhao, Z. Hong, H. Zhou, Y. Yang, *Nano Today* **2015**, *10*, 355.
- [248] A. Fakhruddin, L. Schmidt-Mende, G. Garcia-Belmonte, R. Jose, I. Mora-Sero, *Adv. Energy Mater.* **2017**, *7*, 1700623.
- [249] J. Shi, X. Xu, D. Li, Q. Meng, *Small* **2015**, *11*, 2472.
- [250] Q. Jiang, X. Zhang, J. You, *Small* **2018**, *14*, 1801154.
- [251] Q. Jiang, L. Zhang, H. Wang, X. Yang, J. Meng, H. Liu, Z. Yin, J. Wu, X. Zhang, J. You, *Nat. Energy* **2017**, *2*, 16177.
- [252] T. Leijtens, G. E. Eperon, S. Pathak, A. Abate, M. M. Lee, H. J. Snaith, *Nat. Commun.* **2013**, *4*, 2885.
- [253] L. Etgar, P. Gao, Z. Xue, Q. Peng, A. K. Chandiran, B. Liu, M. K. Nazeeruddin, M. Grätzel, *J. Am. Chem. Soc.* **2012**, *134*, 17396.
- [254] A. Mei, X. Li, L. Liu, Z. Ku, T. Liu, Y. Rong, M. Xu, M. Hu, J. Chen, Y. Yang, M. Grätzel, H. Han, *Science* **2014**, *345*, 295.
- [255] F. Giordano, A. Abate, J. P. Correa Baena, M. Saliba, T. Matsui, S. H. Im, S. M. Zakeeruddin, M. K. Nazeeruddin, A. Hagfeldt, M. Grätzel, *Nat. Commun.* **2016**, *7*, 10379.
- [256] M. Saliba, T. Matsui, J. Y. Seo, K. Domanski, J. P. Correa-Baena, M. K. Nazeeruddin, S. M. Zakeeruddin, W. Tress, A. Abate, A. Hagfeldt, M. Grätzel, *Energy Environ. Sci.* **2016**, *9*, 1989.
- [257] J.-Y. Seo, R. Uchida, H.-S. Kim, Y. Saygili, J. Luo, C. Moore, J. Kerrod, A. Wagstaff, M. Eklund, R. McIntyre, N. Pellet, S. M. Zakeeruddin, A. Hagfeldt, M. Grätzel, *Adv. Funct. Mater.* **2018**, *28*, 1705763.
- [258] A. Abrusci, S. D. Stranks, P. Docampo, H. L. Yip, A. K. Jen, H. J. Snaith, *Nano Lett.* **2013**, *13*, 3124.
- [259] J. Peng, Y. Wu, W. Ye, D. A. Jacobs, H. Shen, X. Fu, Y. Wan, T. Duong, N. Wu, C. Barugkin, H. T. Nguyen, D. Zhong, J. Li, T. Lu, Y. Liu, M. N. Lockrey, K. J. Weber, K. R. Catchpole, T. P. White, *Energy Environ. Sci.* **2017**, *10*, 1792.
- [260] Y. Wang, J. Wan, J. Ding, J. S. Hu, D. Wang, *Angew. Chem., Int. Ed.* **2019**, *58*, 9414.
- [261] Y. Zhu, K. Deng, H. Sun, B. Gu, H. Lu, F. Cao, J. Xiong, L. Li, *Adv. Sci.* **2018**, *5*, 1700614.
- [262] H. Zhou, Q. Chen, G. Li, S. Luo, T. B. Song, H. S. Duan, Z. Hong, J. You, Y. Liu, Y. Yang, *Science* **2014**, *345*, 542.
- [263] T. Bu, J. Li, F. Zheng, W. Chen, X. Wen, Z. Ku, Y. Peng, J. Zhong, Y. B. Cheng, F. Huang, *Nat. Commun.* **2018**, *9*, 4609.
- [264] R. Chen, J. Cao, Y. Duan, Y. Hui, T. T. Chuong, D. Ou, F. Han, F. Cheng, X. Huang, B. Wu, N. Zheng, *J. Am. Chem. Soc.* **2019**, *141*, 541.
- [265] T. Wang, D. Ding, H. Zheng, X. Wang, J. Wang, H. Liu, W. Shen, *Sol. RRL* **2019**, *3*, 1900045.
- [266] M. Saliba, J. P. Correa-Baena, C. M. Wolff, M. Stollerfoht, N. Phung, S. Albrecht, D. Neher, A. Abate, *Chem. Mater.* **2018**, *30*, 4193.
- [267] M. Park, J. Y. Kim, H. J. Son, C. H. Lee, S. S. Jang, M. J. Ko, *Nano Energy* **2016**, *26*, 208.
- [268] X. Liu, Y. Zhang, L. Shi, Z. Liu, J. Huang, J. S. Yun, Y. Zeng, A. Pu, K. Sun, Z. Hameiri, J. A. Stride, J. Seidel, M. A. Green, X. Hao, *Adv. Energy Mater.* **2018**, *8*, 1800138.
- [269] W. Ke, D. Zhao, C. Xiao, C. Wang, A. J. Cimaroli, C. R. Grice, M. Yang, Z. Li, C.-S. Jiang, M. Al-Jassim, K. Zhu, M. G. Kanatzidis, G. Fang, Y. Yan, *J. Mater. Chem. A* **2016**, *4*, 14276.

- [270] E. H. Anaraki, A. Kermanpur, L. Steier, K. Domanski, T. Matsui, W. Tress, M. Saliba, A. Abate, M. Grätzel, A. Hagfeldt, J.-P. Correa-Baena, *Energy Environ. Sci.* **2016**, 9, 3128.
- [271] Q. Dong, Y. Shi, C. Zhang, Y. Wu, L. Wang, *Nano Energy* **2017**, 40, 336.
- [272] W. Q. Wu, D. Chen, Y. B. Cheng, R. A. Caruso, *Sol. RRL* **2017**, 1, 1700117.
- [273] X. Liu, K.-W. Tsai, Z. Zhu, Y. Sun, C. C. Chueh, A. K. Y. Jen, *Adv. Mater. Interfaces* **2016**, 3, 1600122.
- [274] C. Wang, D. Zhao, C. R. Grice, W. Liao, Y. Yu, A. Cimaroli, N. Shrestha, P. J. Roland, J. Chen, Z. Yu, P. Liu, N. Cheng, R. J. Ellingson, X. Zhao, Y. Yan, *J. Mater. Chem. A* **2016**, 4, 12080.
- [275] J. Xie, K. Huang, X. Yu, Z. Yang, K. Xiao, Y. Qiang, X. Zhu, L. Xu, P. Wang, C. Cui, D. Yang, *ACS Nano* **2017**, 11, 9176.
- [276] Y. Bai, Y. Fang, Y. Deng, Q. Wang, J. Zhao, X. Zheng, Y. Zhang, J. Huang, *ChemSusChem* **2016**, 9, 2686.
- [277] L. Xiong, M. Qin, G. Yang, Y. Guo, H. Lei, Q. Liu, W. Ke, H. Tao, P. Qin, S. Li, H. Yu, G. Fang, *J. Mater. Chem. A* **2016**, 4, 8374.
- [278] G. Yang, H. Lei, H. Tao, X. Zheng, J. Ma, Q. Liu, W. Ke, Z. Chen, L. Xiong, P. Qin, Z. Chen, M. Qin, X. Lu, Y. Yan, G. Fang, *Small* **2017**, 13, 1601769.
- [279] M. Abdi-Jalebi, Z. Andaji-Garmaroudi, S. Cacovich, C. Stavrakas, B. Philippe, J. M. Richter, M. Alsari, E. P. Booker, E. M. Hutter, A. J. Pearson, S. Lilliu, T. J. Savenije, H. Rensmo, G. Divitini, C. Ducati, R. H. Friend, S. D. Stranks, *Nature* **2018**, 555, 497.
- [280] F. Zheng, W. Chen, T. Bu, K. P. Ghiggino, F. Huang, Y. Cheng, P. Tapping, T. W. Kee, B. Jia, X. Wen, *Adv. Energy Mater.* **2019**, 9, 1901016.
- [281] D. Yang, R. Yang, K. Wang, C. Wu, X. Zhu, J. Feng, X. Ren, G. Fang, S. Priya, S. F. Liu, *Nat. Commun.* **2018**, 9, 3239.
- [282] J. You, C. C. Chen, L. Dou, S. Murase, H. S. Duan, S. A. Hawks, T. Xu, H. J. Son, L. Yu, G. Li, Y. Yang, *Adv. Mater.* **2012**, 24, 5267.
- [283] R. Gao, Z. Liang, J. Tian, Q. Zhang, L. Wang, G. Cao, *RSC Adv.* **2013**, 3, 18537.
- [284] J. Tian, Q. Zhang, E. Uchaker, R. Gao, X. Qu, S. Zhang, G. Cao, *Energy Environ. Sci.* **2013**, 6, 3542.
- [285] L. Zuo, Z. Gu, T. Ye, W. Fu, G. Wu, H. Li, H. Chen, *J. Am. Chem. Soc.* **2015**, 137, 2674.
- [286] M. M. Tavakoli, R. Tavakoli, P. Yadav, J. Kong, *J. Mater. Chem. A* **2019**, 7, 679.
- [287] P. Chen, X. Yin, M. Que, Y. Yang, W. Que, *RSC Adv.* **2016**, 6, 57996.
- [288] J. Cao, B. Wu, R. Chen, Y. Wu, Y. Hui, B. W. Mao, N. Zheng, *Adv. Mater.* **2018**, 30, 1705596.
- [289] M. Tai, X. Zhao, H. Shen, Y. Guo, M. Zhang, Y. Zhou, X. Li, Z. Yao, X. Yin, J. Han, X. Li, H. Lin, *Chem. Eng. J.* **2019**, 361, 60.
- [290] D. Zheng, G. Wang, W. Huang, B. Wang, W. Ke, J. L. Logsdon, H. Wang, Z. Wang, W. Zhu, J. Yu, M. R. Wasielewski, M. G. Kanatzidis, T. J. Marks, A. Facchetti, *Adv. Funct. Mater.* **2019**, 29, 1900265.
- [291] C. Cetin, P. Chen, M. Hao, D. He, Y. Bai, M. Lyu, J.-H. Yun, L. Wang, *Adv. Sustainable Syst.* **2018**, 2, 1800032.
- [292] J. Y. Jeng, K. C. Chen, T. Y. Chiang, P. Y. Lin, T. D. Tsai, Y. C. Chang, T. F. Guo, P. Chen, T. C. Wen, Y. J. Hsu, *Adv. Mater.* **2014**, 26, 4107.
- [293] Y. Bai, H. Chen, S. Xiao, Q. Xue, T. Zhang, Z. Zhu, Q. Li, C. Hu, Y. Yang, Z. Hu, F. Huang, K. S. Wong, H.-L. Yip, S. Yang, *Adv. Funct. Mater.* **2016**, 26, 2950.
- [294] J. H. Kim, P. W. Liang, S. T. Williams, N. Cho, C. C. Chueh, M. S. Glaz, D. S. Ginger, A. K. Jen, *Adv. Mater.* **2015**, 27, 695.
- [295] J. W. Jung, C. C. Chueh, A. K. Jen, *Adv. Mater.* **2015**, 27, 7874.
- [296] W. Nie, H. Tsai, J. C. Blancon, F. Liu, C. C. Stoumpos, B. Traore, M. Kepenekian, O. Durand, C. Katan, S. Tretiak, J. Crochet, P. M. Ajayan, M. Kanatzidis, J. Even, A. D. Mohite, *Adv. Mater.* **2018**, 30, 1703879.
- [297] W. Chen, F. Z. Liu, X. Y. Feng, A. B. Djurišić, W. K. Chan, Z. B. He, *Adv. Energy Mater.* **2017**, 7, 1700722.
- [298] S. E. Derenzo, E. Bourret-Courchesne, Z. Yan, G. Bizarri, A. Canning, G. Zhang, *J. Lumin.* **2013**, 134, 28.
- [299] X. Zheng, B. Chen, J. Dai, Y. Fang, Y. Bai, Y. Lin, H. Wei, X. C. Zeng, J. Huang, *Nat. Energy* **2017**, 2, 17102.
- [300] W. Luo, C. Wu, D. Wang, Y. Zhang, Z. Zhang, X. Qi, N. Zhu, X. Guo, B. Qu, L. Xiao, Z. Chen, *ACS Appl. Mater. Interfaces* **2019**, 11, 9149.
- [301] T. Bu, J. Li, W. Huang, W. Mao, F. Zheng, P. Bi, X. Hao, J. Zhong, Y.-B. Cheng, F. Huang, *J. Mater. Chem. A* **2019**, 7, 6793.
- [302] Q. Jiang, Y. Zhao, X. Zhang, X. Yang, Y. Chen, Z. Chu, Q. Ye, X. Li, Z. Yin, J. You, *Nat. Photonics* **2019**, 13, 460.
- [303] M. Wang, B. Li, J. Yuan, F. Huang, G. Cao, J. Tian, *ACS Appl. Mater. Interfaces* **2018**, 10, 37005.
- [304] Y. Zou, H.-Y. Wang, Y. Qin, C. Mu, Q. Li, D. Xu, J.-P. Zhang, *Adv. Funct. Mater.* **2019**, 29, 1805810.
- [305] D. Luo, W. Yang, Z. Wang, A. Sadhanala, Q. Hu, R. Su, R. Shivanna, G. F. Trindade, J. F. Watts, Z. Xu, T. Liu, K. Chen, F. Ye, P. Wu, L. Zhao, J. Wu, Y. Tu, Y. Zhang, X. Yang, W. Zhang, R. H. Friend, Q. Gong, H. J. Snaith, R. Zhu, *Science* **2018**, 360, 1442.
- [306] Q. Jiang, Z. Chu, P. Wang, X. Yang, H. Liu, Y. Wang, Z. Yin, J. Wu, X. Zhang, J. You, *Adv. Mater.* **2017**, 29, 1703852.
- [307] Y. Zhao, Q. Li, W. Zhou, Y. Hou, Y. Zhao, R. Fu, D. Yu, X. Liu, Q. Zhao, *Sol. RRL* **2019**, 3, 1800296.
- [308] Y. Shao, Z. Xiao, C. Bi, Y. Yuan, J. Huang, *Nat. Commun.* **2014**, 5, 5784.
- [309] T. Niu, J. Lu, R. Munir, J. Li, D. Barrit, X. Zhang, H. Hu, Z. Yang, A. Amassian, K. Zhao, S. F. Liu, *Adv. Mater.* **2018**, 30, 1706576.
- [310] P. Qin, J. Zhang, G. Yang, X. Yu, G. Li, *J. Mater. Chem. A* **2019**, 7, 1824.
- [311] F. Tan, H. Tan, M. I. Saidaminov, M. Wei, M. Liu, A. Mei, P. Li, B. Zhang, C. S. Tan, X. Gong, Y. Zhao, A. R. Kirmani, Z. Huang, J. Z. Fan, R. Quintero-Bermudez, J. Kim, Y. Zhao, O. Voznyy, Y. Gao, F. Zhang, L. J. Richter, Z. H. Lu, W. Zhang, E. H. Sargent, *Adv. Mater.* **2019**, 31, 1807435.
- [312] J. Peng, J. I. Khan, W. Liu, E. Ugur, T. Duong, Y. Wu, H. Shen, K. Wang, H. Dang, E. Aydin, X. Yang, Y. Wan, K. J. Weber, K. R. Catchpole, F. Laquai, S. De Wolf, T. P. White, *Adv. Energy Mater.* **2018**, 8, 1801208.
- [313] Y. Hou, Z. R. Zhou, T. Y. Wen, H. W. Qiao, Z. Q. Lin, B. Ge, H. G. Yang, *Nanoscale Horiz.* **2019**, 4, 208.
- [314] D. Bi, C. Yi, J. Luo, J. D. Décoppet, F. Zhang, S. M. Zakeeruddin, X. Li, A. Hagfeldt, M. Grätzel, *Nat. Energy* **2016**, 1, 16142.
- [315] M. M. Tavakoli, D. Bi, L. Pan, A. Hagfeldt, S. M. Zakeeruddin, M. Grätzel, *Adv. Energy Mater.* **2018**, 8, 1800275.
- [316] W. Li, M. U. Rothmann, A. Liu, Z. Wang, Y. Zhang, A. R. Pascoe, J. Lu, L. Jiang, Y. Chen, F. Huang, Y. Peng, Q. Bao, J. Etheridge, U. Bach, Y. B. Cheng, *Adv. Energy Mater.* **2017**, 7, 1700946.
- [317] K. Chen, Q. Zhong, W. Chen, B. Sang, Y. Wang, T. Yang, Y. Liu, Y. Zhang, H. Zhang, *Adv. Funct. Mater.* **2019**, 29, 1900991.
- [318] H. Wang, H. Bian, Z. Jin, L. Liang, D. Bai, Q. Wang, S. F. Liu, *Sol. RRL* **2018**, 2, 1800216.
- [319] Y. Wang, T. Zhang, M. Kan, Y. Li, T. Wang, Y. Zhao, *Joule* **2018**, 2, 2065.
- [320] Y. Wang, T. Zhang, M. Kan, Y. Zhao, *J. Am. Chem. Soc.* **2018**, 140, 12345.
- [321] J. Yuan, C. Bi, S. Wang, R. Guo, T. Shen, L. Zhang, J. Tian, *Adv. Funct. Mater.* **2019**, 29, 1906615.
- [322] Y. Wang, M. I. Dar, L. K. Ono, T. Zhang, M. Kan, Y. Li, L. Zhang, X. Wang, Y. Yang, X. Gao, Y. Qi, M. Grätzel, Y. Zhao, *Science* **2019**, 365, 591.
- [323] Q. Zeng, X. Zhang, X. Feng, S. Lu, Z. Chen, X. Yong, S. A. T. Redfern, H. Wei, H. Wang, H. Shen, W. Zhang, W. Zheng, H. Zhang, J. S. Tse, B. Yang, *Adv. Mater.* **2018**, 30, 1705393.
- [324] B. Li, Y. Zhang, L. Fu, T. Yu, S. Zhou, L. Zhang, L. Yin, *Nat. Commun.* **2018**, 9, 1076.

- [325] J. Lu, S. C. Chen, Q. Zheng, *ACS Appl. Energy Mater.* **2018**, *1*, 5872.
- [326] J. Yuan, L. Zhang, C. Bi, M. Wang, J. Tian, *Sol. RRL* **2018**, *2*, 1800188.
- [327] B. Li, C. Fei, K. Zheng, X. Qu, T. Pullerits, G. Cao, J. Tian, *J. Mater. Chem. A* **2016**, *4*, 17018.
- [328] C. Bi, S. V. Kershaw, A. L. Rogach, J. Tian, *Adv. Funct. Mater.* **2019**, *29*, 1902446.
- [329] J. R. Zhang, D. L. Bai, Z. W. Jin, H. Bian, K. Wang, J. Sun, Q. Wang, S. Z. Liu, *Adv. Energy Mater.* **2018**, *8*, 1703246.
- [330] H. Ishihara, S. Sarang, Y. C. Chen, O. Lin, P. Phummirat, L. Thung, J. Hernandez, S. Ghosh, V. Tung, *J. Mater. Chem. A* **2016**, *4*, 6989.
- [331] J. G. Tait, S. Manghooli, W. Qiu, L. Rakocevic, L. Kootstra, M. Jaysankar, C. A. Masse de la Huerta, U. W. Paetzold, R. Gehlhaar, D. Cheyns, P. Heremans, J. Poortmans, *J. Mater. Chem. A* **2016**, *4*, 3792.
- [332] A. T. Barrows, A. J. Pearson, C. K. Kwak, A. D. F. Dunbar, A. R. Buckley, D. G. Lidzey, *Energy Environ. Sci.* **2014**, *7*, 2944.
- [333] M. Yang, Z. Li, M. O. Reese, O. G. Reid, D. H. Kim, S. Siol, T. R. Klein, Y. Yan, J. J. Berry, M. F. A. M. van Hest, K. Zhu, *Nat. Energy* **2017**, *2*, 17038.
- [334] Y. Deng, X. Zheng, Y. Bai, Q. Wang, J. Zhao, J. Huang, *Nat. Energy* **2018**, *3*, 560.
- [335] F. Ye, H. Chen, F. Xie, W. Tang, M. Yin, J. He, E. Bi, Y. Wang, X. Yang, L. Han, *Energy Environ. Sci.* **2016**, *9*, 2295.
- [336] H. Chen, F. Ye, W. Tang, J. He, M. Yin, Y. Wang, F. Xie, E. Bi, X. Yang, M. Gratzel, L. Han, *Nature* **2017**, *550*, 92.